This paper was reviewed and published in Acta Astronautica, Vol 173, August 2020, pp. 91-110 and can be referenced as such! https://doi.org/10.1016/j.actaastro.2020.02.002. This document represents the last status before journal editing, which unfortunately was not performed as requested leaving the second half of the paper in random disorder. The interested reader is therefore invited to read and share this unabridged and correctly formatted version.

Size Matters - The Shell Lander Concept for Exploring Medium-Size Airless Bodies

Christian D. Grimm[a]*, Lars Witte[a], Silvio Schröder[a], Kai Wickhusen[b]

[a] *German Aerospace Center (DLR), Institute of Space Systems, Robert-Hooke-Str.7, 28359 Bremen, Germany,*

[b] *German Aerospace Center (DLR), Institute of Planetary Research, Rutherfordstraße 2, 12489 Berlin, Germany,*

* Corresponding Author, christian.grimm@dlr.de

Abstract

Once addressed as a side topic in planetary exploration, the investigation of small solar system bodies has now become one of the corner stones in the international science community in order to study the formation of the solar system and the evolution of life within. For rendezvous spacecraft, small carry-on landers have proven to be valuable assets, and to have a positive impact on the overall mission cost, by avoiding additional complexity of the main satellite and transferring the risk of close surface maneuvers entirely or at least to some extend to an independent deployable system. However, carry-on landers have been designed currently to land on very small bodies only, but medium-size class objects between diameters of 10 - 50 km are of great interest as well. In this paper we classify carry-on landers with respect to their touchdown and operational strategy, evaluate the constraints of ballistic deployments for different target bodies as well as identify the niche for using simple honeycomb impact dampers compared to optional retro-propulsion systems. Further, we introduce the system design of an attitude- stabilized Shell Lander using a generic instrument carrier attached to a single ejectable crash-pad with stabilizing capability to protect the instrument carrier from structural damage, limit internal shock loads for sensitive payloads as well as reduce the amount of bounces on the surface. Finally, we present a mission architecture for a reference case to the Martian moon Phobos as well as provide a proof of concept based on laboratory impact tests and a multi-body simulation to analyze touchdown dynamics including terrain interaction, shell-shedding and bouncing.

Keywords: (Asteroid Landing, Payload Delivery, Impact Energy Absorption, Shell Lander, Ejectable Crash-Pad,)

1. Introduction

In recent years, the exploration of small solar system bodies has increased significantly. Apart from remote sensing surveys and fly-bys, especially landing and sample collection missions have dramatically increased our understanding of their physical composition as well as their mechanical properties. Small carry-on landers, like the European Rosetta lander Philae [1] which successfully landed on comet 67P/Churyumov/ Gerasimenko on November 12th, 2014, or the German/French lander MASCOT [2][3] on-board the Japanese Hayabusa2 mission (Fig. 1) which successfully landed on asteroid 162173 Ryugu on October 3rd, 2018, have proven to be a valuable assets by avoiding additional complexity of the main satellite and keeping project development times and costs in manageable bounds.

Landing on small bodies is particular difficult due to the weak gravitational field and means to secure the lander to the surface have to be taken into account. However, with increasing size and density of the target the gravitational attraction on a lander increases also. Currently, non-propelled landers have been designed to land on very small bodies only, but medium-size class objects between diameters of 10 - 50 *km* are of great interest as well. For example, the Martian moons Phobos (D = 22 *km*) and Deimos (D = 12.5 *km*) as well as many Main-belt or Jupiter Trojan asteroids have mean diameters of more than 10 *km*. Rendezvous missions to those targets considering a detachable lander will have to focus on a dedicated landing support system. Depending on the capabilities of the mother spacecraft and resulting landing strategy, mainly the separation altitude defines the final landing velocity at touchdown. Higher landing velocities introduce high shock loads and can cause damage to lander subsystems and instruments. Reducing the need of an optional retro-propulsion system, other means of cancelling the descent Δv such as absorbing the impact energy have to be taken into careful consideration. Non-propelled landing strategies can be divided into three categories.

(i) Landing without a dedicated landing subsystem for very low touchdown velocities (e.g. MASCOT),
(ii) Landing with energy absorption to reduce the impact velocity to stay below the target's escape velocity (e.g. Philae), and
(iii) Heavy duty landing with a dedicated protection system to lower internal shock loads.

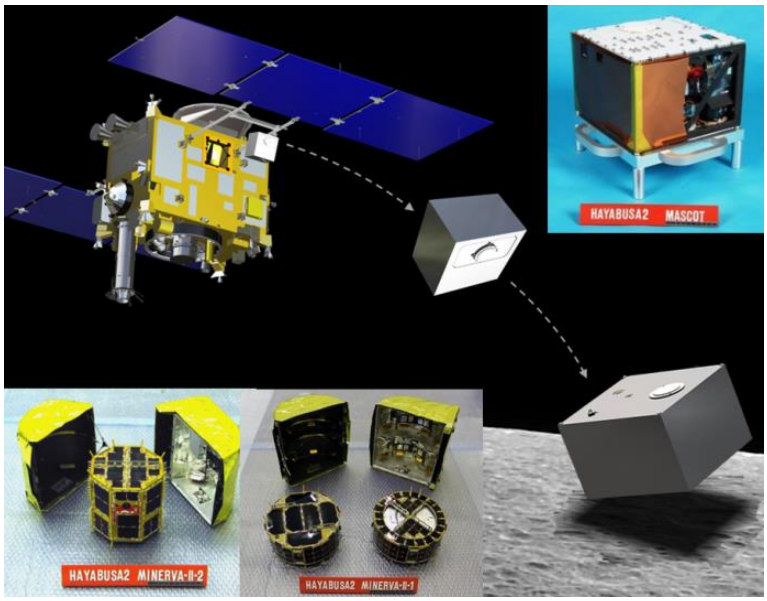

Fig. 1: Landing on Small Bodies. Example from the Hayabusa2 mission including 4 deployable landers

In order to enable the exploration and landing on medium-size airless bodies, this paper outlines the concept of advancing small body landers with a crushable-shell protection system to sustain higher landing velocities in the range of 1 - 5 *m/s*. Design aspects as well as possible reference missions are given in addition to results of initial crushable-shell impact tests.

2. Application and Reference Missions

The increased interest for small body science is seen not only by the scientific results already gained by passed missions and the expected outcome of current flight missions, but also by the continuous effort of the international scientific community to propose and to undertake missions to small bodies. Such missions can be characterized by four partially interlinked sub-disciplines, (i) *Solar System and Asteroid Science*, (ii) *Planetary Defence*, (iii) *Human Exploration* and (iv) *Resource Utilisation* [4]. In recent years another sub-discipline, *Mining and Exploitation* of asteroids for rare materials, became also a bit more of attention. However, with the current price tag on space missions and involving time durations a justifiable concept has yet to be put forward.

Current selected missions, addressing one or more of the above topics, include the Double Asteroid Redirect Test (DART) from NASA/APL targeting to impact on the secondary of a binary asteroid (proposed launch Dec. 2020), the Lucy Jupiter Trojan multiple target rendezvous mission from NASA Goddard/SwRI (proposed launch Oct. 2021), the Psyche space probe to a metal-rich M-class asteroid by NASA/JPL/ASU (proposed launch mid 2022) and the Mars Moon eXplorer (MMX) by JAXA (proposed launch Sep. 2024) targeting the two moons of Mars, Phobos and Deimos. A European proposal to accompany the DART mission, the Asteroid Impact Monitor (AIM), was original not selected, but is currently being reinstated as Hera [5] to observe the aftereffects of the DART impact (proposed launch Oct.2023).

Typically, small body missions, be it fly-bys, orbiting spacecraft or landing systems are big space probes, whose development costs range in the hundreds of million US$ for small-class missions up to more than a billion US$ for high priority flagship missions. For example, several *Small Body Missions* have been performed by NASA within its small-class mission Discovery Program, which range between 300-500M$ (completed missions: NEAR, Deep Impact, Stardust and Dawn; planned missions: Psyche and Lucy) [6][7]. The currently running New Frontiers medium-class mission OSIRIS-REx has a cost cap of 850M$ plus launch vehicle [8] and the European Rosetta mission, a cornerstone mission within ESA's Horizon 2000 Program, came with a price tag of approximately 1.5B$ [9]. However, specifically the carry-on landers can avoid additional complexity of the main satellite and transferring the risk (and cost) of close surface maneuvers entirely or at least to some extend to an independent deployable system. Generally, small instrument packages and dedicated landers can scientifically enhance a main mission by either providing ground truth for the mission's orbital investigations, exploring niches on the surface too difficult or too risky to be reached for the main satellite, or adding complementary in-situ investigations with higher and long-stable resolution [10][11].

Good examples for this are the MINERVA and MASCOT landers on the Hayabusa and Hayabusa2 mission. Other concepts worth mentioning are the POGO concept from the Applied Physics Laboratory (APL) [12], the Hedgehog platform from the Jet Propulsion Laboratory (JPL) [13][14] as well as the advanced MASCOT-2 design from the German Aerospace Center (DLR) which has been proposed in the frame of the ESA AIM mission [15][16]. The advancement and further development of carry-on systems has the potential to further stimulate low cost participation in planetary exploration and increase the science return of any mission exploring these unique solar system bodies.

The aspect of lowering the overall cost of missions to main-belt and near-Earth objects, as well as the benefits to include smaller carry-on smallsats, explicitly including the addition of a lander asset, has recently been addressed also in the Small Planetary Platforms (SPP) assessment performed by ESA [17] in Nov-Dec. 2017 as well as in Jan. 2018. This study was to evaluate a possible "tool box" of technical building blocks that the community can use to develop new planetary missions consisting of a mothership spacecraft carrying a swarm of smallsats to be deployed for multi-point science observations within a cost range of up to 150M€ (175M$). For such mission architectures, these "assets" will need to be as flexible and robust as possible to cope with varying science and mission constraints.

3. Classification of Small Body Landers

Due to the fact that only a few small body landings have been attempted and even less have been successful (see Table 1), a comprehensive classification of this type of landing system is rather difficult. At the time of writing, 13 attempts have been made to put a man-made object onto the surface of a low gravity body (with 8 of these being successful). One mission is currently in operation planning for a touch-and-go maneuver in order to take surface samples. One mission is currently in development and out of multiple pure academic design studies 3 are being regarded as having reached an high enough technological readiness level (TRL) to be considered for an upcoming small body mission. In order to find similarities and to identify key technologies an evaluation is made based on these 18 past, present and possible future landers.

A primary parameter here is the kinetic energy at touchdown (TD), which is defined as the work done by a lander with mass ***m*** when decelerating from its incoming speed ***v*** to a state of rest

$$E_k = \frac{1}{2} \cdot m \cdot v^2 \qquad (1)$$

Using this equation, the data from Table 1 is plotted in Fig. 2 which reveals cluster in specific regimes summarized additionally in Fig. 3. The easiest distinction of Small Body Landers (SBL) is between Orbiter Landers and Carry-on Landers. Orbiter landers are the complete probe (or final separated stage) of a rendezvous spacecraft which is intended to make physical contact with the target either during a planned mission operation or as an end of life strategy. Orbiter landers use their on-board attitude control thrusters and other reaction controls like fly wheels in order to reduce and limit the contact speed (e.g. NEAR, Fobus Grunt, Rosetta, MMX). A special case is given by touch-and-go samplers which, strictly speaking, do not actually land, but only touch the surface with some form of extended sample mechanism (e.g. Hayabusa 1+2, OSIRIS REx). Carry-on landers do rely on an orbiter spacecraft by which they are carried to the specified target. Once arrived, they are separated in order to make the remaining journey towards the surface independently. All carry-on landers which have either been flown to date or have been seriously studied did not use or take retro-propulsion systems into account, since landing speeds were low enough that the final Δv could safely be made by impact forces only. Naturally, if for some future mission design the limit for high TD velocities will be reached a dedicated deceleration system using conventional thrusters will be the usual way forward. As it is shown in Fig. 2 and Fig. 3, carry-on landers can further be divided with respect to their operational and touchdown strategy into mobile *soft*, *mobile robust* and *stationary landers* and are being either TD controlled or TD un-controlled. Mobile soft landers are usually small surface instruments without attitude control and with very low impact Δv. The corresponding shock acceleration at surface contact, after a tumbling descent, is some orders of magnitude lower than the endured shock and vibration environment of a given launcher system. No structural reinforcement, impact attenuation or special landing support system is necessary. Up until now all soft landers did incorporate some form of mobility concept to either upright after landing or to move across the surface to enlarge the scientific area (e.g. MINERVA 1+2, MASCOT 1+2, Hedgehog).

A variation of mobile landers designed to survive higher landing velocities is found in mobile robust landers, where the harder landing is taken by a reinforced outer casing (e.g. PrOP-F, POGO).

Table 1: Past, present and possible future Small Body Landers

Mission	Target	Lander	Carry-on	System Mass [kg]	Launch	Landing	TD vel [m/s]	Ref
Fobos 1	Phobos	Fobos 1 DAS	yes	67	07.07.88	N/A	< 1	[18]
Fobos 2		Fobos 2 DAS	yes		12.07.88	N/A	< 1	
(CCCP)		Fobos 2 PrOP-F	yes	50		N/A	< 1	
NEAR (NASA)	Eros	orbiter	-	820 (wet), ~500 (at TD)	17.02.96	12.02.01	~1.6	[18]
Hayabusa	Itokawa	orbiter	-	510 (wet), ~450 (at TD)	09.05.03	19.11.05	~0.03	[19]
(JAXA)		MINERVA	yes	0.5		N/A	~0.1	[20]
Rosetta	Chury-G.	orbiter	-	2900 (wet), ~1300 (at TD)	02.03.04	30.09.16	~1	[1]
(ESA)		Philae	yes	96		12.11.14	~1	
Fobos-Grunt (Russia)	Phobos	lander stage	-	1820 (wet), ~750 (at TD)	08.11.11	N/A	~0.5	[21]
Hayabusa2	Ryugu	orbiter	-	609 (wet), ~550 (at TD)	14.12.14	22.02.19	~0.03	[22] [47][48]
(JAXA)		MINERVA-II-1a+b	yes	2 x 1.1		21.09.18	~0.2	
		MINERVA-II-2	yes	1		08-10.10.19	~0.5	
		MASCOT	yes	10		03.10.18	~0.2	
OSIRIS-Rex (NASA)	Bennu	orbiter	-	2110 (wet), ~1500 (at TD)	08.09.16	2020 (TBC)	~0.1	[8] [23]
MMX (JAXA)	Phobos	lander stage	-	3400 (wet), ~1500 (at TD)	09.2024	~2025	~1	[24]
TBD	TBD	MASCOT-2 (DLR)	yes	13	-	-	< 0.3	
TBD	TBD	Hedgehog (JPL)	yes	25	-	-	< 0.5	[25] [26]
TBD	TBD	POGO (APL)	yes	10	-	-	5 (TBC)	[12]

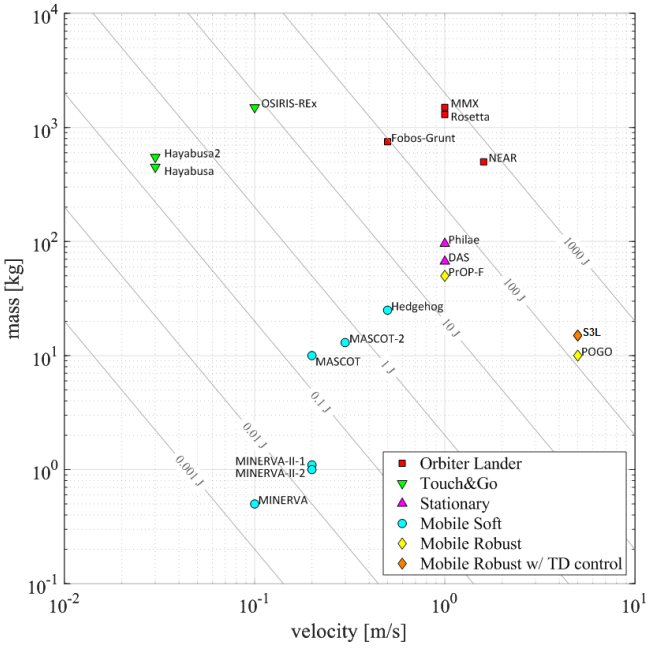

Fig. 2: Touchdown velocity-mass-diagram indicating the touchdown energy for certain types of SBL systems (underlying data from Table 1, display adapted from [26]) for low gravity bodies.

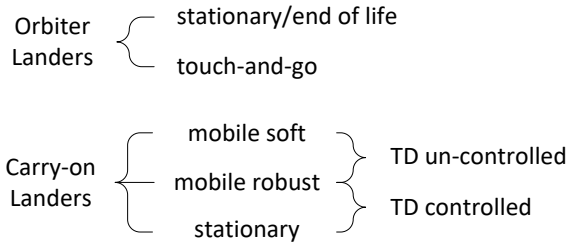

Fig. 3: Clustering of SBL systems with respect to touch-down and operational concept

Stationary systems (one surface contact only) also take the impact energy into account. But in contrast to mobile robust systems, the descent is stabilized and directed (TD control) so that the surface contact is made with a defined orientation. They have to entirely absorb the impact energy and/or counteract the rebound after surface contact. Usually a combination of different subsystems is used including landing gears, internal impact dampers, hold-down thrusters and surface anchors (e.g. DAS, Philae). If this TD control principle is applied to the mobile systems we find another sub-category, *mobile robust with touchdown control*. Like the mobile robust

systems, which have no attitude control, they incorporate some form of relocation mechanism. But since the TD is directed only the particular area which is intended to make the first physical contact with the surface needs to be equipped with a special damper or absorber system. This latter concept, however, has up until now neither been flown or studied. For this reason, this paper introduces the concept of a Single-axis Stabilized Shell Lander (SSSL or 3SL). In the following section the application niche in the Δv regime is identified where impact protection by mechanical dampers and absorbers remain beneficial for a use without additionally required propulsive Δv reduction.

4. *Rationale and application niche*

Honeycomb material, mainly from aluminum alloys, has already a long tradition as reliable energy absorption means for impact and crash attenuation application. Its energy absorption capability comes from deliberately buckling, collapsing and plastic deformation of the hexagonal walls of the cells when loaded. The compression strength required to crush it is determined by the size and the aluminum foil gauges used to form the honeycomb cells. Crush strength and bulk density are designed, type-specific properties of such honeycomb material. The crush strength of commercially available aluminum (alloy 5052 and 5056) honeycomb samples [28] is plotted over its bulk density in Fig. 4 below. Regression curves are plotted additionally, showing that the crush strength is – roughly – proportional to the square of the material's bulk density ($\boldsymbol{\sigma \propto \rho^2}$). We use this relation to make a basic assessment of the mass efficiency of honeycomb material if used as decelerator for a small landing probe.

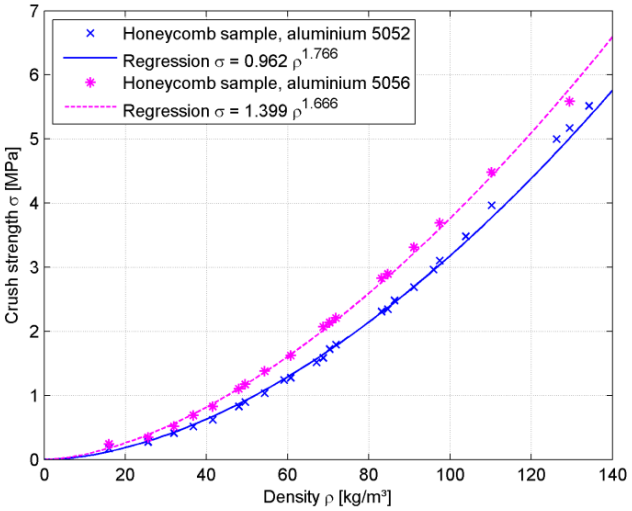

Fig. 4: Crush strength dependence as function of honeycomb bulk density. Data points of samples taken from [28]

Let $\boldsymbol{E_k}$ be the kinetic energy at touchdown with $\boldsymbol{m_{total}}$ the total mass which is the combined mass of the to-be-delivered system $\boldsymbol{m_{sys}}$ and the required crushable absorber mass $\boldsymbol{m_{cr}}$. The kinetic energy shall be absorbed through plastic deformation of the shell such that $\mathbf{E_k = E_{plast}}$.

$$E_k = \frac{1}{2} m_{total} \cdot v^2 = F_{cr} \cdot s = \sigma \cdot \underbrace{A \cdot s}_{:=V_{cr}} = E_{plast} \qquad (2)$$

The latter is the product of the crush force $\boldsymbol{F_{cr}}$ and the deformation stroke $\boldsymbol{s}$. The crush force in turn is the product of the honeycomb material's crush strength $\boldsymbol{\sigma}$ and the contact area $\boldsymbol{A}$. For a symmetrical absorber with a constant contact area (e.g. cuboid or cylinder), the parameters $\boldsymbol{A}$ and $\boldsymbol{s}$ represent also the crushing volume $\boldsymbol{V_{cr}}$. The crush volume can be expressed as a function of the crush strength σ and crushable mass $\boldsymbol{m_{cr}}$ using the functional relation $\boldsymbol{\sigma \approx k \cdot \rho^2}$ as shown in Fig. 4.

$$V_{cr} = \frac{m_{cr}}{\rho} = \sqrt{\frac{k}{\sigma}} \cdot m_{cr} \qquad (3)$$

This expression can be reformulated as the mass ratio of the required crushable mass $\boldsymbol{m_{cr}}$ with regard to the system's mass $\boldsymbol{m_{sys}}$ as a function of the landing velocity or Δv respectively.

$$\frac{m_{cr}}{m_{sys}} = \frac{\Delta v^2}{2\sqrt{k\sigma} - \Delta v^2} \qquad (4)$$

This equation has a singularity at

$$\Delta v = [2 \cdot (k \cdot \sigma)^{0.5}]^{0.5} \qquad (5)$$

where the mass ratio of $\boldsymbol{m_{cr}}$ to $\boldsymbol{m_{sys}}$ rises to infinity. Travelling with this Δv a piece of honeycomb material contains more kinetic energy than can be absorbed in a deliberate, controlled manner by intended collapsing of its honeycomb cells. Obviously, the use of such material becomes extremely inefficient when approaching this limit Δv. This limit is however dependent to the respective materials crush strength.

For comparison reasons, a similar expression has been derived from the classical rocket equation using a propulsion subsystem to decelerate the landing probe.

$$\frac{m_{prop}}{m_{sys}} = 1 + \lambda - e^{-\Delta v/(I_{sp} \cdot g_0)} \qquad (6)$$

In equation (6) the "decelerator mass" $\boldsymbol{m_{prop}}$ is composed of the fixed propulsion subsystem mass and the Δv-dependent propellant mass. The fixed subsystem mass representing the tank, tubes and regulators and the thruster is expressed as a mass share $\boldsymbol{\lambda}$. The figure $\boldsymbol{\lambda}$ – assumed to be $\boldsymbol{\lambda \approx 0.1}$ – is

approximated using the mass budget values available from off-the-shelf cube sat propulsion hardware. For this application a cold gas system with a specific impulse of 60s is assumed. An overview of such propulsion systems is given in [29] and a particular application to small body missions is studied in [30]. Although these propulsion cube sat hardware is developed primarily for orbiting elements, it is assumed here that it can be adapted in principal to deliver a shorter but higher thrust braking burn for the purpose of landing.

The resulting mass ratios expressed in equation (4) and (6) as function of landing Δv of both crushable and propulsive means are plotted in Fig. 5. The Δv regime with the crushable materials mass ratio being lower than its benchmark for a propulsion subsystem marks the niche where a crushable shell can offer an advantage in terms of mass efficiency. Not accounted are associated mass contributions from the respective structural or mounting support and any required guidance and control subsystem. A full trade-off must include also additionally factors such as mission design flexibility and system reliability. Due to its simplicity, in the following sections the application niche for this shell lander technology is exploited to design a highly reliable delivery system for a small asteroid landing probe.

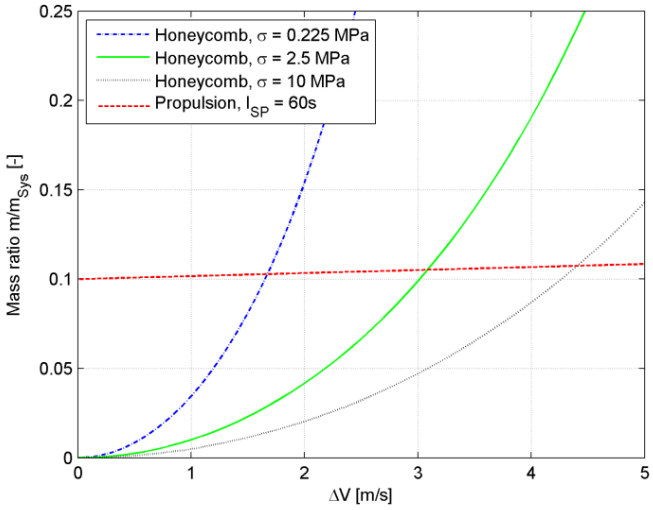

Fig. 5: Mass ratios of decelerator mass – crushable shell with different crush strength and propulsion using cold gas – shown as function of landing Δv

5. Constraints and Limitations

Without retro-propulsion for deceleration, the landing speed of a carry-on lander is entirely dependent by Newtons law of gravity. The higher and therefore the longer the free fall within a gravitational field the higher the impact velocity. Up to now carry-on landers have been designed to and been successfully proven for vertical touchdown velocities of 0 - 1 m/s. This included on the lower end soft landers without impact attenuation, and on the upper end landers with impact attenuation and hold down/anchor systems. From historical experience of other planetary landing systems (e.g. Moon and Mars) it is known to which residual vertical landing speed a system has to be decelerate in order to perform a "soft landing" that does not result in damage or destruction of the vehicle or anything on board (~ 5 m/s) [27].

The gravitational environment of a target body is determined by its mass defined foremost by its size but also by its bulk density which depends on the bodies material composition and its internal structure. The density is related to the object's spectral type. Estimations presented in [31] give mean bulk densities of the three main classifications C, S, and M type asteroids as 1.38 ±0.02, 2.71 ±0.02, and 5.32 ±0.07 g/cm^3, respectively. Comets are less dense as they are mainly composed of water ice, dust and other frozen volatiles. In addition, they commonly have large macro-porosities of > 60% forming large voids inside suggesting bulk densities of less than 1.0 g/cm^3, with a most likely value of 0.6 ±0.2 g/cm^3 [32]. This becomes apparent when comparing the values in Fig. 6, showing the relation of the targets size and respective surface acceleration.

For example, Bennu (BEN), B-type, having a slightly lower surface acceleration than Itokawa (ITO), S-type, although being 50% larger. Didymos (DID), S-type, having a slightly higher surface acceleration than comet Churyumov/Gerasimenko (C-G) although being only a quarter of its size. The gravitational influence of the target is one of the primary factors determining the design of a small body lander. Depending on the gravitational potential $\boldsymbol{g}$ and the deployment altitude $\boldsymbol{h}$ estimates of the landing velocity $\boldsymbol{v}$ can be made. In a constant gravity environment this can be determined by balancing the potential energy $\boldsymbol{E_p}$ at release with the kinetic energy at impact $\boldsymbol{E_k}$.

$$E_k = E_p \Leftrightarrow \frac{1}{2}mv^2 = m \cdot g \cdot h \qquad (7)$$

As the lander will not lose any mass during its descent we could simplify this to

$$v = \sqrt{2gh} \qquad (8)$$

However, if the target bodies are small or the separation altitude is much larger than the radius of the target body we have to account for varying acceleration. Since the gravitational attraction is in this case not constant. For this, we have to integrate the equation of motion which is given by Newton's law of gravity describing that the target body with mass $\boldsymbol{M}$ and the lander with mass $\boldsymbol{m}$ will attract each other with a combined force of

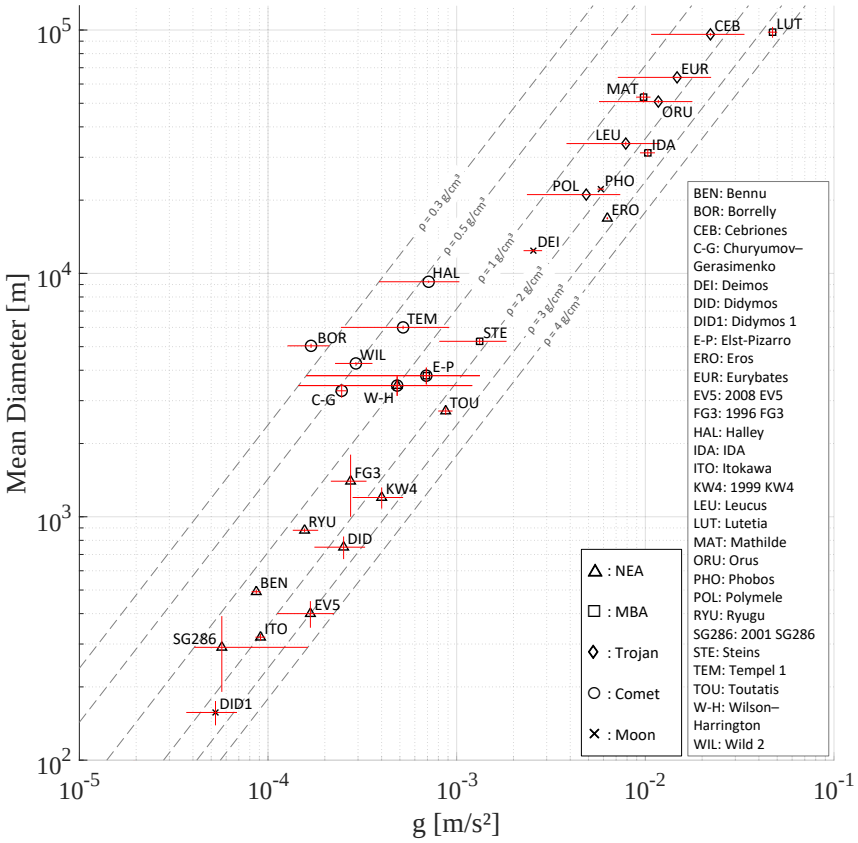

Fig. 6: Log-log plot of the gravitational attraction with respect to mean diameter and bulk density of possible target objects including error margins [33]

$$F = \frac{GMm}{r^2} = m \cdot a \tag{9}$$

where G is the gravitational constant and r is the distance towards the centers of gravity. As a is the acting acceleration on the lander we get the equation of motion within the gravity field towards the surface by

$$g = a = \frac{dv}{dt} = \frac{GM}{r^2} \tag{10}$$

Multiplying with v and integrating we get the expression for the total energy of the two objects

$$E = \frac{1}{2}v^2 + \frac{GM}{r} \tag{11}$$

where the first part is again the kinetic energy and the second part the potential energy. And as energy is always conserved the value for the energy at the moment of separation has to be the same value as the energy at the moment of impact ($\mathbf{E_{sep}} = \mathbf{E_{imp}}$). Using now the values for the respective moment in time we get the amount of energy at separation with

$$E_{sep} = \frac{1}{2}{v_0}^2 + \frac{GM}{r} \tag{12}$$

where r is the radius of the target body and v_0 is the initial velocity given to the lander, which is a combination of the relative velocity of the spacecraft and the eject velocity of the separation mechanism. The energy at impact is then given respectively with

$$E_{imp} = \frac{1}{2}{v_{imp}}^2 + \frac{GM}{r_0} \tag{13}$$

where r_0 is the distance from the point of separation towards the gravity center of the target body and v_{imp} the terminal velocity at impact. Solving for v_{imp} we are left with the expression

$$v_{imp} = \sqrt{{v_0}^2 + 2GM\left(\frac{1}{r} - \frac{1}{r_0}\right)} \tag{14}$$

accounting for both varying acceleration and non-vanishing initial velocity. Setting v_0 to be 0 and r_0 to be infinite we get the expression for the targets escape velocity on its surface.

$$v_{esc} = \sqrt{\frac{2GM}{r}} \tag{15}$$

This is also the gravitational limit of the impact speed v_{lim} for a ballistic lander which can only be surpassed when $v_0 > 0$ and is of the same magnitude as v_{imp}. For really small targets, it is advisable to ensure $v_{imp} < v_{esc}$ to avoid a scenario where the lander bounces off the surface and gets lost into space. For bigger targets, solving equation (14) instead for the separation altitude $h = r_0 - r$ we get the expression

$$h_{max} = \frac{r^2(v_{max}^2 - v_0^2)}{2GM - r(v_{max}^2 - v_0^2)} \qquad (16)$$

to determine the maximal allowable deployment height hmax for a maximal allowable impact velocity vmax. And finally, with a target simplified as a spherical and symmetric body of mass M, expressed by its volume V and bulk density ρ

$$M = V \cdot \rho = \frac{4}{3}\pi r^3 \cdot \rho \qquad (17)$$

we can now transform equation (15) into

$$v_{esc} = \sqrt{\frac{8G\pi r^2}{3} \cdot \rho} \qquad (18)$$

And respectively from equation (10) we get the magnitude of the targets gravitational potential with

$$g_{target} = \frac{4G\pi r}{3} \cdot \rho \qquad (19)$$

With this we have now all expressions to analyze the impact velocity of a lander, separated at a given altitude over a target body expressed in terms of size and density.

Fig. 7 shows the estimation of impact velocity with respect to surface acceleration and deployment height for the MASCOT-1 lander on asteroid Ryugu, the Rosetta lander Philae on comet Churyumov/ Gerasimenko and a possible future carry-on lander to the Martian moon Phobos. Possible scenarios for varying deployment altitudes are given in addition to the targets respective escape velocities. According to equation (14) and the respective target size and density the velocity increase during the free fall to the surface can vary greatly between a few centimeters to meters per second. For small bodies of a few hundred meters in diameter and resulting low gravities the initial separation velocity determines to great effect the resulting touch down speed, which both are of the same order of magnitude as the escape velocity of the body. This was in fact the case for the landing of Philae, where the impact speed was slightly higher as the targets escape velocity (due to the relative high initial speed) [1]. But this was than fortunately damped both by the soft surface as well as the internal electro-mechanical damper system. This effect weakens as the targets grow bigger as here the velocity increase due to the higher gravitational free fall acceleration dominates. However, this means also that even at low deployment altitudes the touchdown speed would rise very quickly to a few m/s. If we take for example a separation altitude of 1 km on Phobos, the vertical touchdown velocity would be already 3.3 m/s. And for this regime of impact velocity one should consider some form of protection to ensure the lander itself is not fractured at impact as well as to reduce the resulting shock acceleration for the landers subsystem, specifically for sensitive instruments like cameras and other optics.

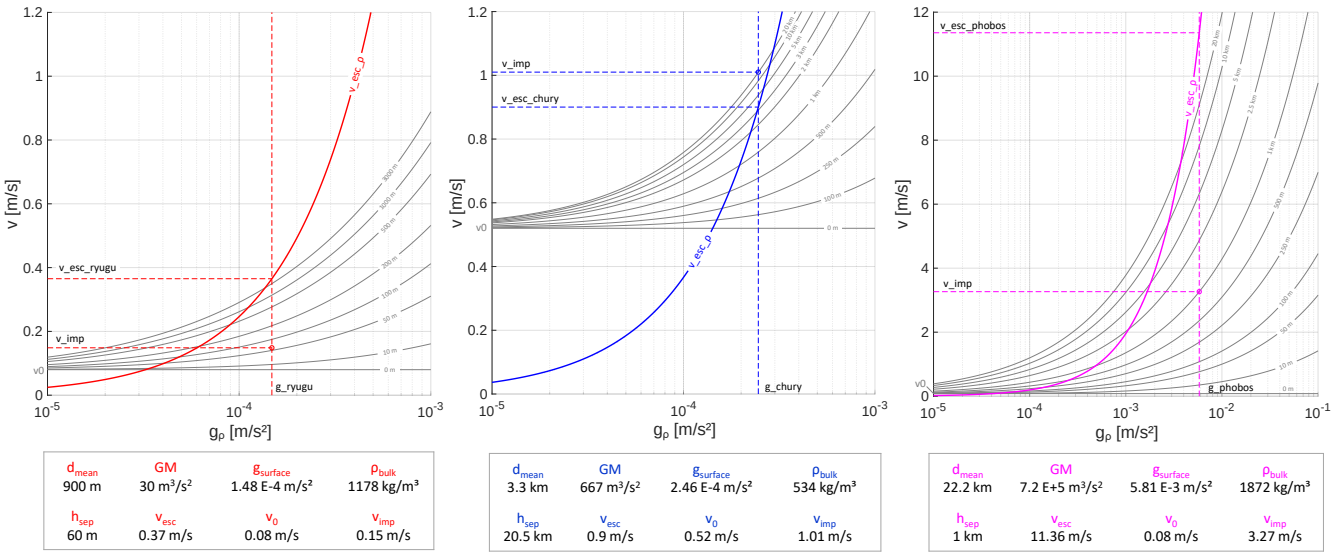

Fig. 7: Estimations of impact velocity with respect to surface acceleration and deployment height for the MASCOT-1 lander on asteroid Ryugu (left), the Philae lander on comet Churyumov/Gerasimenko (center) and a possible future carry-on lander to the Martian moon Phobos (right).

6. Mission Analysis and Concept of Operation

Using the Martian moon Phobos as a reference case being both a good example for the class of a medium-size airless body as well as being a scientifically interesting target object we present in the following a mission analysis and concept of operation for the delivery of the proposed shell lander.

With the strongly perturbing gravity of Mars and the mass of Phobos being too small to capture a satellite, it is not possible to orbit the Martian moon in the usual sense. However, orbits of a special kind – generally referred to as distant retrograde orbits, also called quasi-satellite orbits (QSO) – exist and can be sufficiently stable to allow several months of operations in the vicinity of the moon. Typical QSO's are only stable for inclinations up to approximately 30° relative to the equator of Phobos and at distances above 20 km relative to the center of the moon. In this simulation we start in a QSO at a closest distance of 25 km and an inclination of 0°. For the Lander delivery we assume a separation height of 1 - 3 km above the surface of Phobos. To reach this altitude the spacecraft will use its thruster and perform maneuvers which bring the spacecraft closer to the surface. In the simulation we decelerated the speed by a $\Delta v = 2$ m/s to bring the spacecraft on a close fly-by course, with the closest distance to the surface < 3 km (see Fig. 8). During the closest approach the speed over ground is approximately 10 m/s. For lander separation a relative speed of < 1 m/s is required. Consequently, before separation the S/C will have to decelerate to that speed over ground and release the lander. Afterwards the spacecraft has to accelerate to the previous flyby speed again and perform an additional maneuver at a distance of 25 km to enter original QSO again. The overall delta-v demand for these 4 maneuvers is $\Delta v < 30$ m/s and will increase to $\Delta v < 60$ m/s for a delivery in the polar area. Directly after separation from the mother spacecraft, the gravity of Phobos will cause a continuously accelerated free fall. Depending on the release altitude, the impact speed and free fall time vary. At 1 km altitude the impact speed after 10 minutes of free falling is about 3 m/s (Fig. 9), while at release altitude of 3 km the lander will fall for 20 minutes and touch the surface with an impact speed of approximately 5 - 6 m/s. (see also Fig. 7).

Fig. 10 shows the concept of the shell lander delivery. As mentioned above, the carrying mother spacecraft will perform a close fly-by with a relative speed above ground. The shell lander will be deployed retrograde against the normal flight path to reduce the horizontal velocity component. Afterwards, the shell lander will perform a ballistic free fall towards the surface (see section 5).

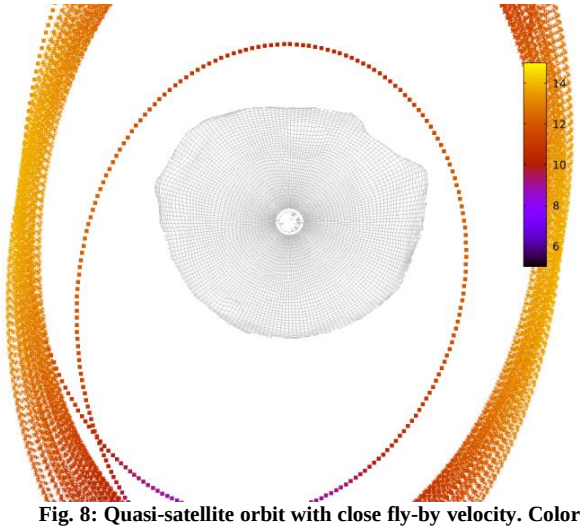

Fig. 8: Quasi-satellite orbit with close fly-by velocity. Color coding in m/s to Phobos surface.

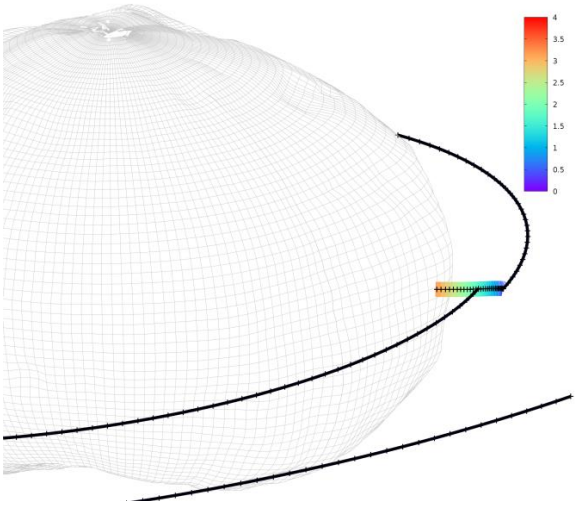

Fig. 9: Lander delivery from close flyby. Color coding in m/s to Phobos surface. Each cross marks one minute.

Since the mobile instrument package has only one protective shell at its bottom side the descent has to be stabilized about the vertical axis. This can be achieved with the aid of a simple single momentum wheel (fly-wheel) within the shell platform. This strategy is inherited by the Rosetta Lander Philae which was also fly-wheel stabilized during its ballistic descent. Details with regard to this strategy are found in [34].

After the free fall and consequent continued acceleration due to the targets gravity, the shell lander will impact onto the surface with a defined velocity in the order of a few meters per second. The kinetic energy at the moment of impact will be absorbed by the plastic deformation of the crushable shell element (crash-pad) as well as in the best case also by the granular displacement of the regolith material.

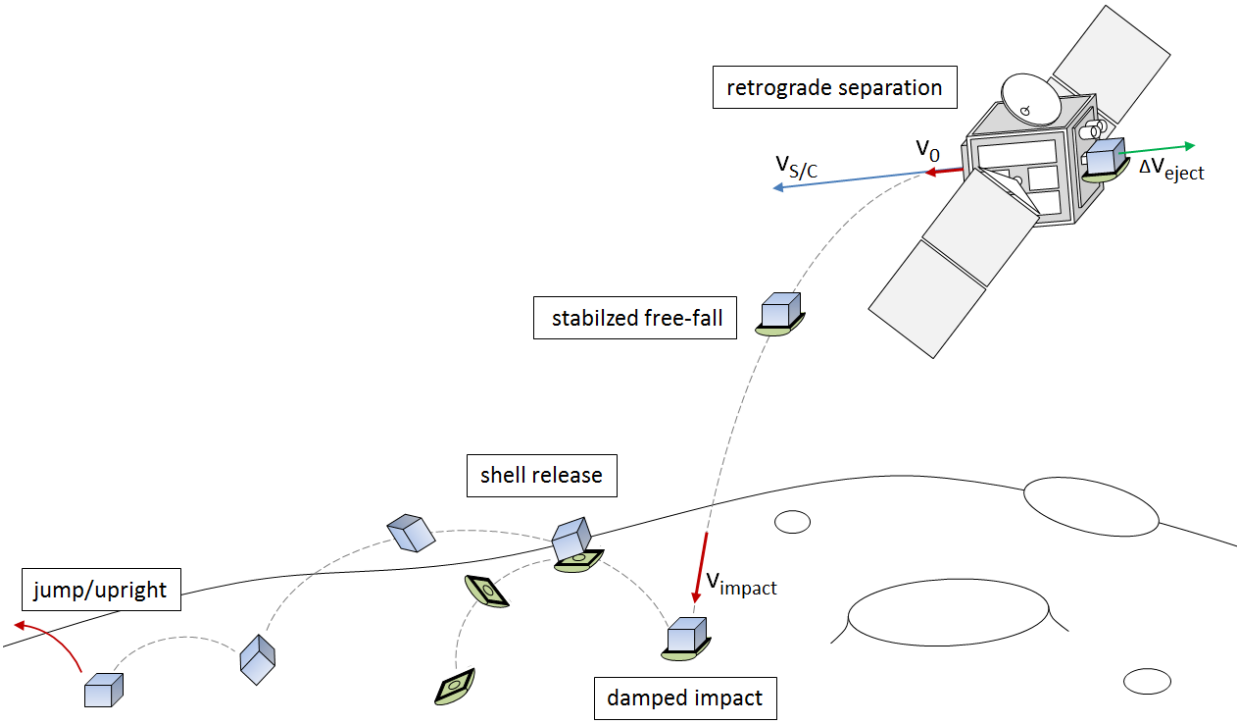

Fig. 10: Concept of operations of the shell lander delivery and touchdown scenario (Mode 1)

This however is not the design case of the crash-pad, since we have to assume that the lander will hit either a flat bare rock or even worse a sharp and solid boulder. The deformation of the crash-pad alone will protect the instrument package from structural damage as well as reduces the resulting shock accelerations within by one or two orders of magnitude (see section 8). This ensures on the one hand the survivability of the carried sensitive instruments and electronics and on the other limits the remaining deflected kinetic energy for the following bouncing phase which reduces the size of the landing ellipse. After the first touchdown and damped impact, the shell platform can either be released directly to free the mobile unit early (Mode-1, Fig. 10) or be kept to damp rolling in order to limit the landing area further (Mode-2). The latter is a concept already proposed by the failed PrOP-F lander which used a wire frame to limit bouncing and uncontrolled rolling over the surface [35][36][37]. The release of the shell would follow in this case after the lander comes to rest. Once freed from the shell, the mobile unit can start its normal surface operation by an up-righting or jump to another location.

7. System Design

To obtain a reference system design we focus on the class of SBL which have recently most often been studied and reported. These are the DLR MASCOT-Type, the APL POGO and the JPL Hedgehog (refer to section 3 for their general classification). All have in common that they are mobile surface assets. In addition to the crushable shells primary task to safely decelerate the lander and attenuate the impact shocks we require here that it must be separated after landing to enable the mobile element an unobstructed further surface operation.

The design of the Single-axis Stabilized Shell Lander (3SL) shown in Fig. 11 is based on a mobile instrument carrier attached to an Ejectable Crash-Pad (ECAP). We present in the following a design concept using the MASCOT-2 lander [15][16] depicted in Fig. 12 as a baseline. But we would like to emphasize that the ECAP design is flexible and can be adapted to support other types of small body landers (see section 7.2).

The main part of the ECAP system is the Crushable Half-Shell (CHS) made of a honeycomb core material glued to a high strength face sheet laminate, which is designed explicitly to the given mission requirements. On top of this shell rests an interface structure with a sandwich plate and a frame of vertical cross beams aligned in an x-pattern, which bear the loads both for the landing impact as well as for the required preload for launch. This interface structure is also the platform on which the supporting

electronics are integrated, including the stabilizing flywheel, the separable umbilical connector (UMC) as well as additional sensors, such as an inertia measurement unit (IMU) or tri-axial accelerometers (3xAcc). This way the ECAP could be used as an instrument itself acquiring data on surface mechanical properties such as the compressive strength and effective E-modulus of the soil, as well as the damping properties between the soil and the lander. The mobile carrier is attached via 4 stand-offs transferring all remaining loads into its primary structure. The mechanical fixation as well as the release capability is ensured via a single non-explosive actuator (NEA), which needs to be allocated within the mobile unit. No additional push-off mechanism is necessary as this is provided by the release of the preload stored within the cross beams as well as the spring contacts inside the UMC. The mass breakdown can be seen in Table 2.

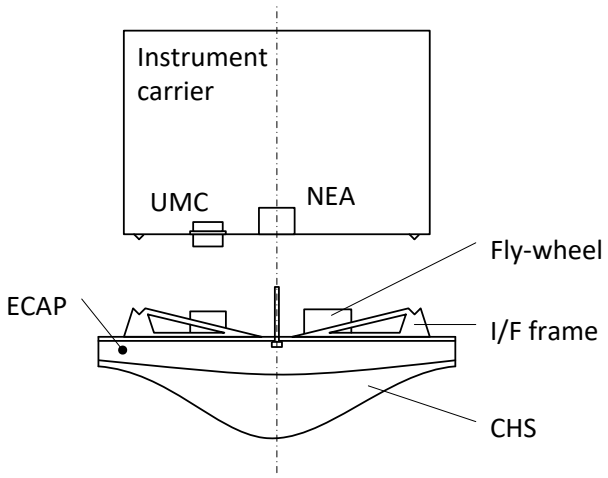

Fig. 11: Single-axis Stabilized Shell Lander (3SL) schematic.

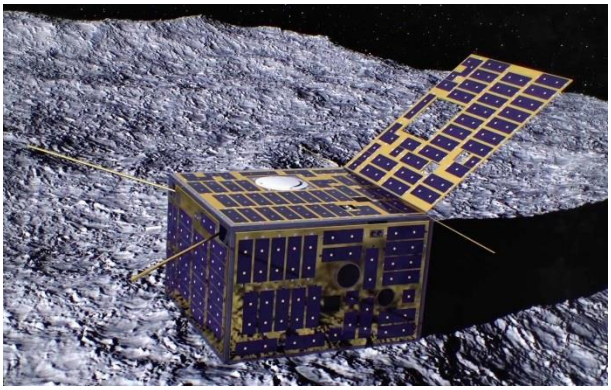

Fig. 12: Artist impression of the MASCOT-2 lander which was developed by DLR and proposed for the ESA AIM mission (image credit: ESA).

Table 2. Mass budget of the shell lander (MASCOT-2 baseline) including the Ejectable Crash Pad (ECAP) and an interface structure for the attachment to a mother spacecraft.

Component	Mass w/o margin [kg]	Maturity margin [%]	Mass w/ margin [kg]
Mobile Instrument Carrier (MASCOT-2)			
Mobility	1.02	9	1.11
GNC	0.44	36	0.60
On-Board Computer	0.56	11	0.62
Communication	0.88	18	1.04
Power Supply	3.43	11	3.81
Structure incl. Solar P.	2.23	20	2.67
Thermal Control	0.22	5	0.23
System Harness	1.33	8	1.44
Payloads	2.01	15	2.31
Sub-total	***12.12***		***13.83***
Landing Sub-System (ECAP)			
CHS	0.500	10	0.55
I/F Plate	0.250	10	0.28
I/F Frame	0.250	20	0.30
NEA incl. bolt	0.080	5	0.08
UMC incl. Harness	0.065	5	0.07
Fly-wheel	0.150	30	0.20
Optional Sensors (e.g. IMU or 3xAcc)	0.020	5	0.02
Sub-total	***1.32***		***1.49***
Spacecraft Interface and Deployment			
Structure	0.45	18	0.53
Harness	0.16	13	0.18
Release and Push-off	0.50	30	0.65
Calibration Targets	0.12	17	0.14
Sub-total	***1.23***		***1.50***
Total landed mass	***13.44***		***15.32***
Total payload mass	***14.67***		***16.82***

7.1. Design Concept

Earlier design concepts included a full-shell enclosure (Fig. 13). This was based on the previous MASCOT-1 design where no attitude control was foreseen and the lander would make a tumbling descent followed by multiple bounces across the surface. Once at rest, the shell would unfold in order to provide unhindered visibility of internal instruments. The here proposed half-shell concept has some advantages. The overall mass and volume is reduced as less crushable elements are needed. The interface to both the mobile lander as well as to the mother spacecraft is less complex. The risk of possible jammed levers or hinges by the impact is removed. And due to the directed descent the impact vector is vertical to the surface requiring mainly uni-axial deformable energy absorption, which matches best the honeycomb core crush performance.

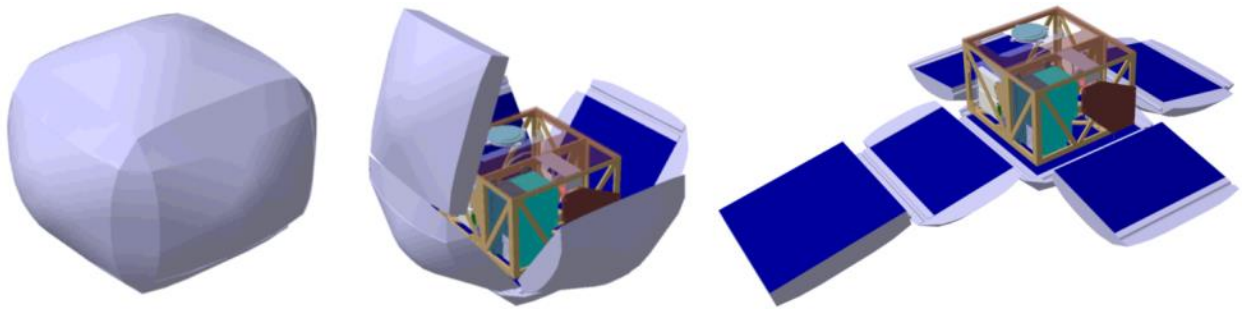

Fig. 13: Early design concept of the shell lander with a full enclosure

Fig. 14 shows the overall size of the 3SL which is 360 x 360 x 340 mm, while the CHS has a maximum height of 100 mm. The width of the CHS is driven by an attitude tolerance of 5°. It is therefore slightly larger than the attached mobile lander to avoid unwanted side contacts. The shape and curvature of the CHS is defined by the touchdown conditions which can range from a flat surface to an impact on an obstacle. From this it follows that the impact does not necessarily go through the Center of Gravity (CoG) as can be seen in Fig. 15. Equation (20) defines the mass distribution for the lander with respect to the distance from its CoG.

As a result, it can be seen in Fig. 16 that the full mass is only acting for a central impact. If the lander hits an obstacle at the edge of the CHS, only 40% of the mass is affecting the crash performance. This provides a "design parameter" for the required thickness of the crushable material. Due to the fact, that an off-centered hit would induce a moment, part of the translational energy is converted into rotational energy which reduces the load onto the material. For this reason and a possible mass optimization, the CHS absorber can be shaped accordingly. Further details can be reviewed in [38] and [39].

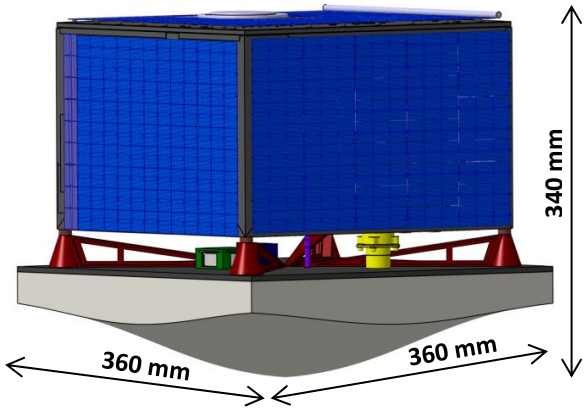

Fig. 14: 3SL concept including a generic mobile instrument carrier attached to the ECAP.

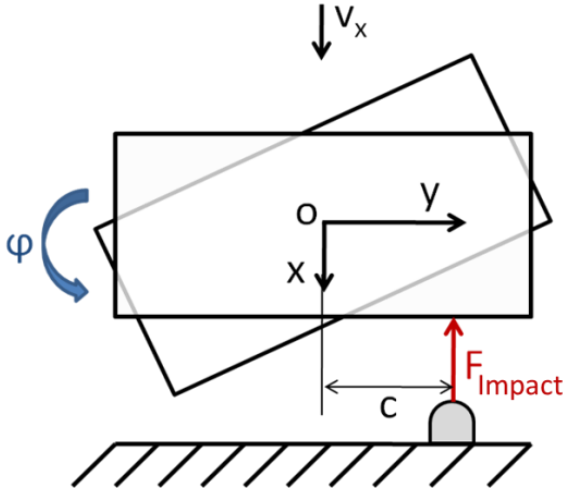

Fig. 15: Scheme for calculating the mass distribution when impacting on an obstacle

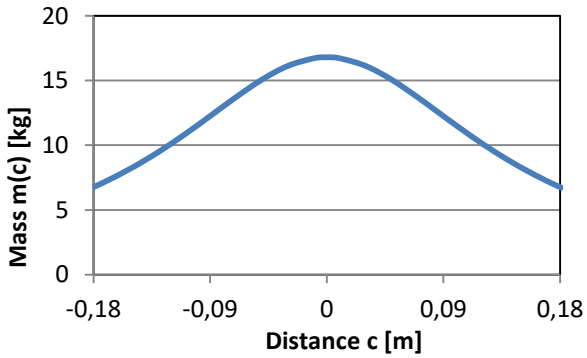

Fig. 16: Calculated mass distribution of the CHS

$$m_{(c)} = \frac{1}{\frac{c^2}{J_{Lander}} + \frac{1}{m_{Lander}}} \qquad (20)$$

Furthermore, it is assumed that any equipment required to implement and to support the landing strategy and which are not used anymore after landing shall be ejected after the CHS has been spent. The flywheel and additional instrumentation is therefore mounted on the ECAP. Instrumentations are sensors which acquire data on the CHS performance such as additional accelerometer and displacement sensors. In that regard this data would support analysis to distinct between soil mechanical observations upon impact and soil contribution to energy absorption as opportunity science. Such sensors are marked as optional in the mass budget.

The vertical cross beams and the supporting electronics are mounted to the sandwich-plate on top of the CHS (Fig. 17) and the required power supply is provided by the mobile carrier via the separable umbilical connector. This connector as well as the NEA are both MASCOT heritage and have been flown successfully on the Hayabusa2 mission (Fig. 18). The proposed flywheel is a standard cubesat component. Commercial examples are presented in Fig. 19.

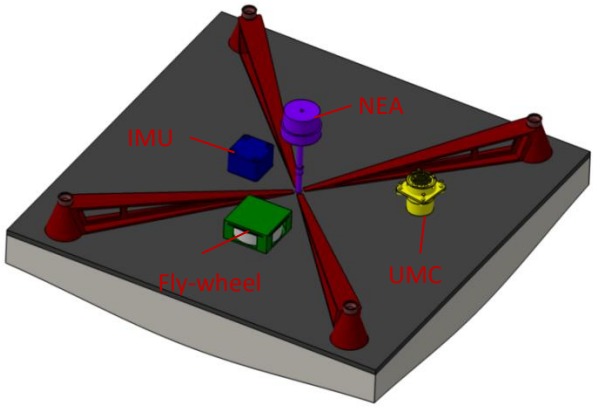

Fig. 17: ECAP platform with its lander interface frame (red) and supporting electronics

Fig. 18: Separation electronics as used in the Hayabusa2/MASCOT mission. Left: NEA model 9100 (image credit NEA Electronics). Right: Umbilical separation connector (UMC).

Fig. 19: Commercial flywheels. Left: MicroWheel (RWP015) from Blue Canyon Technologies. Right: CubeWheel Medium from CubeSatShop.com

7.2. Compatibility to other Mobile Landers

As mentioned above, the ECAP design is flexible and its underlying concept is intended to support the landing of mobile surface elements in general. In a "What-If"-study we briefly assess the application also to the JPL Hedgehog and the APL POGO. The interface design can be adapted to hold either of these landers. A comparing sketch is given in Fig. 20. Each type of lander would need to be equipped with a NEA or similar hold down and release mechanism (HDRM) and requires the capability to send a high but very short impulse current (e.g. via the internal battery) in order to activate the release. For the MASCOT-2 and POGO landers a separable umbilical connector would provide power supply for the fly-wheel as well as data interface for any attached sensors. The Hedgehog lander on the other hand has the advantage, that it can make use of its already integrated tri-axial momentum wheels which are used primarily for locomotion across the surface. Here, no additional fly-wheel or connector is required reducing the total mass of the shell platform. The resulting system mass, including the addition of a spacecraft interface and push-off mechanism for initial deployment is presented in Table 3.

Table 3: The mass breakdown of 3 different types of mobile landers equipped with the ECAP and an estimated S/C interface and push-off mechanism.

	APL POGO	**DLR MASCOT-2**	**JPL Hedgehog**
Lander	10 kg	13.8 kg	25 kg
ECAP platform	1.5 kg	1.5 kg	1.2 kg
S/C Interface and Push-off (not shown, but estimated)	1.5 kg	1.5 kg	1.8 kg
Total landed mass	**11.5 kg**	**15.3 kg**	**26.2 kg**
Total system mass	**13 kg**	**16.8 kg**	**28 kg**

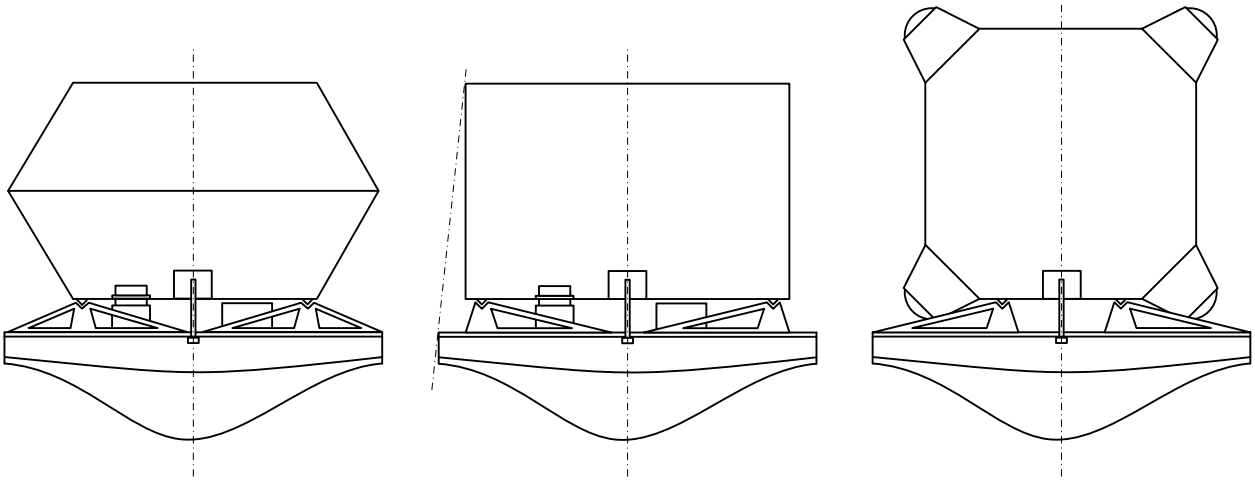

Fig. 20: Comparing sketch (to scale) showing the ECAP attached to various mobile landers, including from left to right the APL POGO, the DLR MASCOT-2 and the JPL Hedgehog

8. Proof of Concept Testing

In order to validate the shell lander concept and to improve the accuracy of our FE analysis we have performed laboratory impact tests at the landing and mobility test facility (LAMA) at DLR Bremen, which is normally used to study and test the landing events of larger landers for Moon and Mars [40][41]. It should be noted, that the main purpose of these tests is to investigate and to confirm the dynamic crush performance as well as the damping behavior (coefficient of restitution) of the used absorber material rather than the dynamic motion response of the lander. One way to test would be to simply drop a test object from a certain height to achieve the desired impact speed. For example, the equivalent drop height for an impact speed of 3 m/s, using equation (8) would be 46 cm. The force vector due to gravity is in this case always vertical.

$$\overrightarrow{F_G} = -mg \qquad (21)$$

However, with a simple drop setup testing a very ductile material like Al-honeycombs as impact absorber, the rebound off the ground after impact cannot precisely be measured. Working against the gravity vector there is either no rebound at all or only a very small one providing a very poor signal to noise ratio. Another way to test is to use a pendulum instead, which is deflected from its vertical rest position to the same height to achieve the same impact speed (Fig. 21).

$$h = L(1 - cos\varphi) \qquad (22)$$

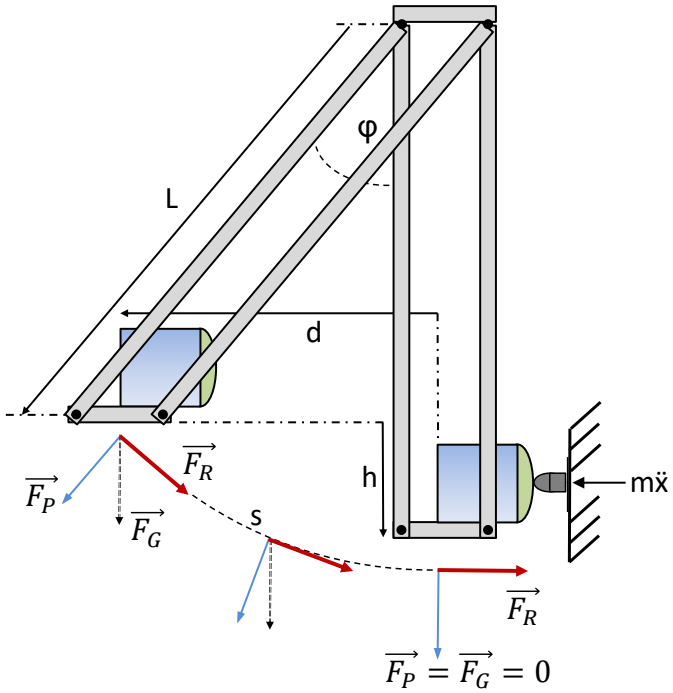

Fig. 21: Rigid parallel pendulum – schematic

The resulting force vector in this case is then a function of deflection angle φ.

$$\overrightarrow{F_R} = -mg\cos\varphi \qquad (23)$$

But the advantage of using a pendulum is that during the moment of impact (φ = 0),

$$\overrightarrow{F_G} = \overrightarrow{F_P} = -mg\ \sin\varphi \qquad (24)$$

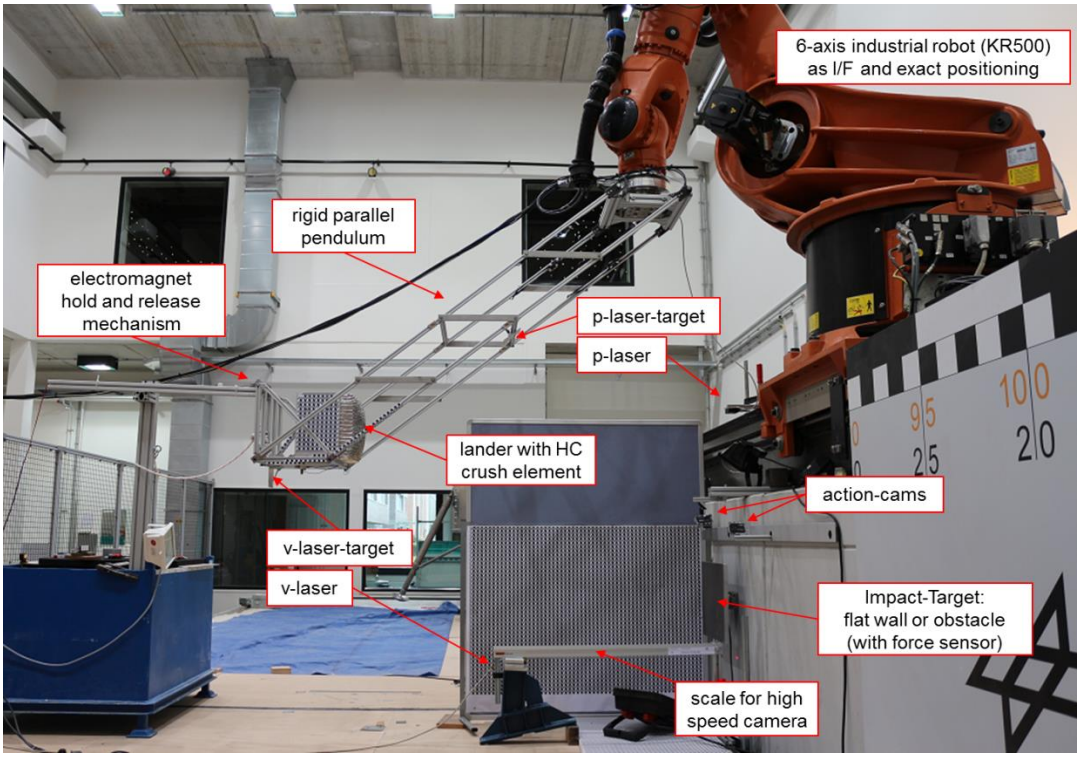

Fig. 22: Pendulum test setup for the shell lander impact tests

becomes 0 and $\boldsymbol{F_R}$ is perpendicular to the gravity vector. The test object is therefore decoupled from gravity and thus reacts only due to the resisting force of the obstacle. In this respect, one can analyze the bouncing effect of the test object when being deflected off the ground or obstacle. The bouncing ratio $\boldsymbol{e}$ or coefficient of restitution (COR) is then determine by

$$e = \frac{v_{out}}{v_{in}} \qquad (25)$$

where $\boldsymbol{v_{in}}$ is the impact velocity just before contact and $\boldsymbol{v_{out}}$ is the deflected velocity just after impact in the opposite direction. This is important when focusing on landing on small bodies with low gravities as this parameter defines for example how big the landing error ellipse will be and how long it takes for the lander to settle on the surface.

As it is shown in Fig. 21 and Fig. 22, the pendulum setup is made of a rigid aluminum (Al) frame forming a parallel-bar pendulum. This technique is used to ensure that the test object is always horizontal and in line with the impact target. In addition, a rigid Al-frame was preferred over ropes or wires to analyze and to account for induced vibrations to the Al-beams (single harmonic and coupled oscillation) during the impact. The decision for this type of test rig was due to experience made in previous tests, where an elastic pendulum with ropes was used (2 translational DoF and 3 rotational DoF). Here, it was observed that the induced vibrations within the ropes (multiple and non-harmonic oscillations) during the impact would superimpose the sensor measurements, which could not simply be filtered out and which reduced the validity of the results (large errors). Hence, the limitation to a 1 DoF test rig, but providing better results for the verification of crash absorber material. For this see also [46].

The setup included a load cell directly behind the impact target, tri-axial accelerometers on the test object, laser range finders as well as high-speed and video cameras to characterize the impact event as well as the pendulum itself. Tests were performed for the expected worst cases,

A. Rigid flat surface: Load case with minimal deformation but highest force and deceleration load. Represents impact on a bare rock or a boulder much larger the size of the lander (Fig. 23, top),

B. Rigid penetrator: Load case with small contact area resulting in lowest force and deceleration load but maximal deformation. Represents impacting on a hard obstacle or a boulder much smaller the size of the lander (Fig. 23, bottom).

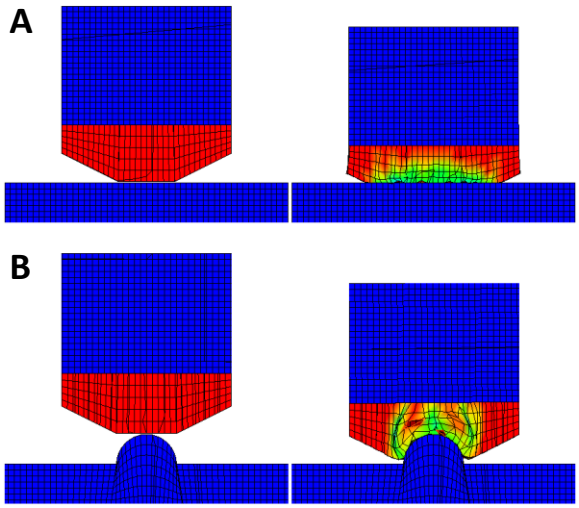

Fig. 23: FE simulation of the CHS (red) attached to a generic lander (blue): A) impact on a flat surface; B) impact on an obstacle

Besides the crush performance of the Al-honeycomb core (σ = 0.1725 MPa), further objectives were to investigate the influence of the face sheet laminates (layers tested: 0, 1 and 2 layers of a Dyneema fabric) as well as the dependence of the impact velocity (velocities tested: 2, 3 and 4 m/s, respectively). Fig. 24 shows impact cases for a sample without a face sheet (top) as well as with a supporting facesheet (bottom).

Fig. 25 - Fig. 30 show exemplary results for impact cases A and B for a crash-pad without a face sheet laminate. For a flat impact the contact area $\boldsymbol{A}$ (see equation (2)) increases quickly due to the curvature of the crash-pad. Consequently, the resistance $\boldsymbol{F_{cr}}$ provided by the target plate is large and the deceleration time and distance $\boldsymbol{s}$ is small. Due to this, the impact force and acceleration are large as well. For a penetrator impact without a face sheet the contact area and therefore the resistance is small and remains constant due to the small and constant cross section. For lower velocities (2 and 3 m/s) the crash-pad was able to prevent the impactor to protrude towards the lander. For higher velocities (e.g. 4 m/s) the crash-pad was not able to stop the impactor from breaking through.

Fig. 31 - Fig. 36 show exemplary results for impact cases A and B for a crash-pad including a face sheet laminate. Similar to the case without a face-sheet, the contact area for a flat impact increases quickly due to the curvature of the crash-pad. Consequently, the resistance provided by the target plate is large and the deceleration time and distance is small. Similarly, the impact force and acceleration are large as well. However, when comparing now the impact case for a penetrator including a face sheet, the contact area increases also, but much slower than for the flat case. Due to this, the impact force and acceleration are higher than for the non-laminate

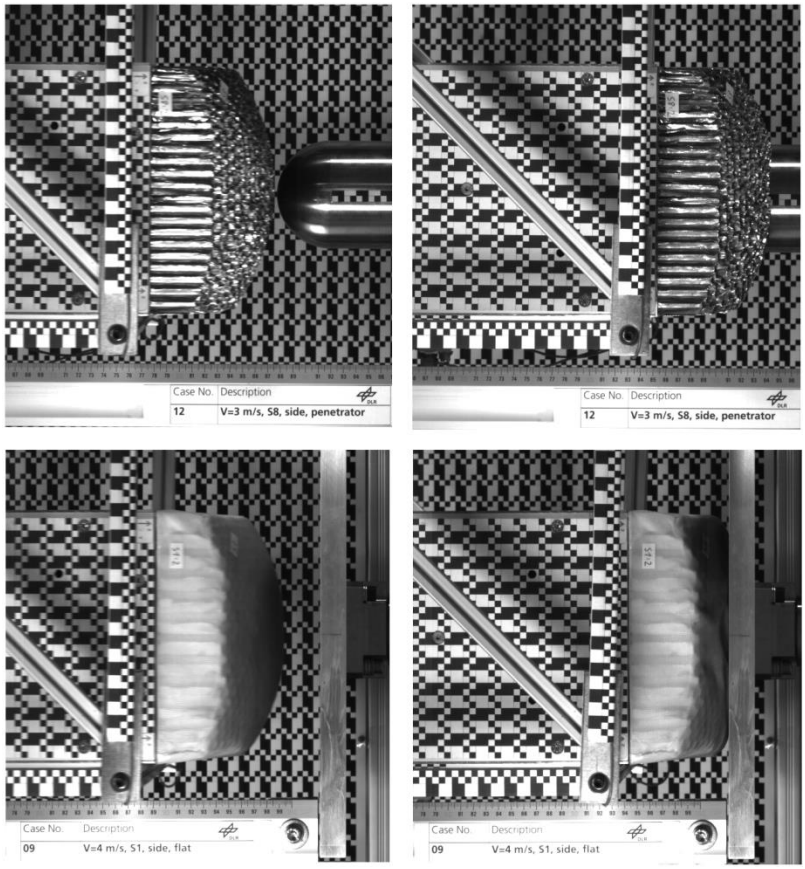

Fig. 24: Top: Test example: penetrator impact w/o face sheet laminate (v=3m/s): before impact (left), after impact (right); Bottom: Test example: flat impact with a face sheet laminate (v=4m/s): before impact (left), after impact (right)

case, but much lower as compared to the flat impact cases since the crash-pad is given more time to spread the impact force via the face sheet over a wider area. Even for high velocity impacts, the face sheet does effectively prevent the impactor to break through. However, the amount of energy being absorbed is higher in the flat impact case compared to the penetrator impact case (see Fig. 38 and Fig. 40). These results match closely the test predictions acquired by FE analysis prior to these tests (see Fig. 23).

As mentioned before, impact cases A and B present worst cases on opposite ends. Flat impacts result in very high acceleration values and penetrator impact cases present a high risk of breaking through the protective shield. They act therefore as boundary condition to which a crash-pad has to be designed to. The face sheet, on the other hand brings these boundaries closer together. With the right combination of resisting core material and face sheet laminate a crash-pad can be designed to ensure both, the capability to protect the lander from structural damage as well as to limit the residual shock acceleration for sensitive instruments on-board. These load cases may seem very conservative since a potential soft regolith is neglected. But as most small body missions are “firsts” the actual surface response can never be known upfront. Therefore, it is best practice in system design to take the more constraining case as a design load case at least in concept development. This of course does not preclude a relaxation of this approach if mission specific factors allow to do so (e.g. apriori knowledge from a previous mission or maybe just higher risk acceptance in program management)

Summarizing results are presented in (Fig. 37 to Fig. 40). Blue squares mark flat impact cases and red triangles mark penetrator impact cases. Test object identifiers describe larger square pads (T) and smaller rectangular pads (S). Indices 0-2 indicate the number of face sheets used. Fig. 37 shows the peak acceleration over varying impact speeds. As mentioned above, for penetrator cases with no-laminate the shock acceleration remains constant as for all other cases the acceleration increases linear with impact speed. Highest values result for flat impacts, lowest values result from penetrator cases. Fig. 38 presents the crush energy (absorbed energy during impact) for varying impact speeds.

From the linear trend of all cases it follows that the value of crush energy, which is also the indicator for the crash-pads performance, is directly and linear dependent from the impact speed. The higher the impact speed and consequently the higher the impact energy, the more energy is absorbed. This means also, that the crush energy is independent from the impact energy. Fig. 40 shows that 75 - 85 % of the kinetic impact energy is absorbed within the crash-pad depending only on the used material combination. In terms of the aforementioned COR, and using face sheet material, these relates to an $\boldsymbol{e}$ of 0.4 – 0.5. This can be reduced further, however, using softer core materials which would also lower peak acceleration values specifically for flat impact cases.

As it was shown above, a central impact would be a worst case scenario where, according to Equation (20), all of the impact energy needs to be damped by the crash cushion. This is ensured by the systems horizontal stabilization during its descent (see section 7.1). However, it can be very likely that due to a significant horizontal velocity component after separation and due to an inclined ground or large obstacle, the touchdown could occur in the form of a glancing contact where an edge of the crash cushion makes the first contact with the ground (see Fig. 39). In such an event, the worst case contact would be similar as for a central contact, where the load path goes directly through the landers center of gravity (c) and no energy gets converted into rotation. For this scenario we have performed tests according to Fig. 42. The edge of the cushion was manufactured with a slightly stiffer AL-honeycomb core material ($\boldsymbol{\sigma}$ = 0.6210 MPa), to account for the shorter length available to be deformed, as well as implemented with a 45° angle to ensure an uniaxial load transmission. As it can be seen in Fig. 41 the crush performance of the edge cases (pen-e, flat-e) are comparable with the respective central cases (pen-c, flat-c). The apparent changes in impact energy were due to setup adaptations during test. However, just like in the results presented in Fig. 40, the flat impacts cause higher accelerations but also higher energy absorption, as volumetric vise more material gets crushed in a shorter time.

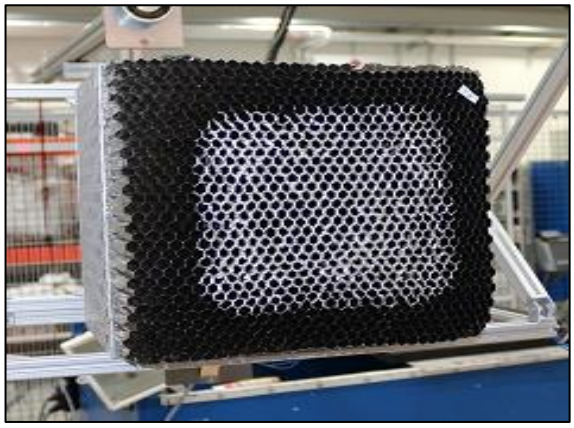

Fig. 25: Crash-pad w/o a face sheet after impact with a hard flat surface (v=4m/s)

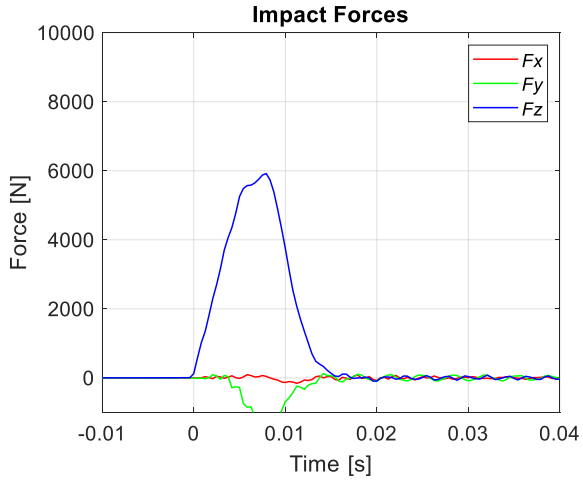

Fig. 26: Impact force, flat impact w/o face sheet (v=4m/s)

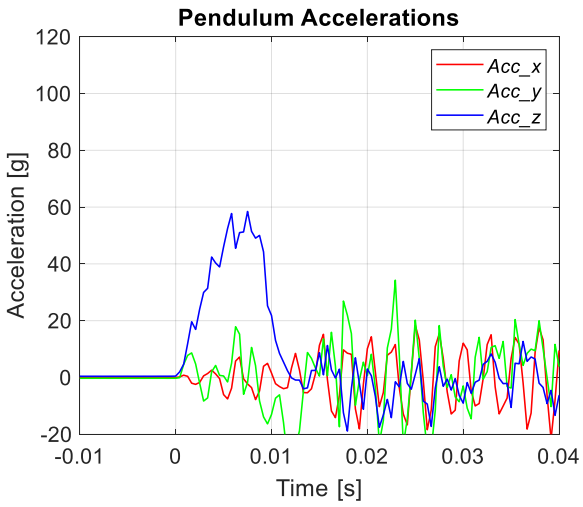

Fig. 27: Impact acceleration, flat impact w/o face sheet (v=4m/s)

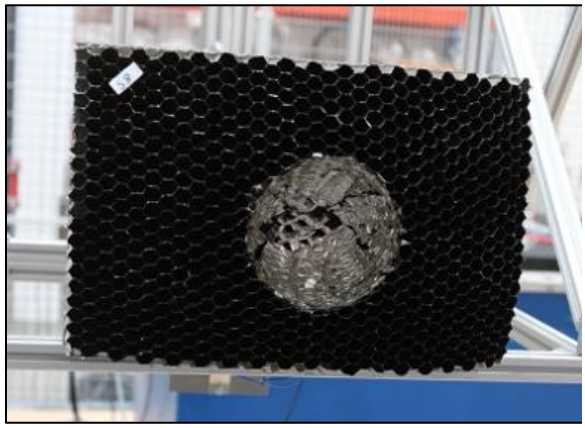

Fig. 28: Crash-pad w/o a face sheet after impact with a hard obstacle/boulder (v=3m/s)

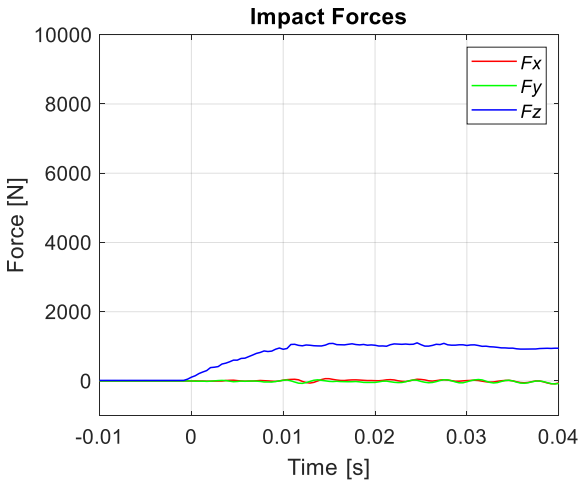

Fig. 29: Impact force, boulder impact w/o face sheet (v=3m/s)

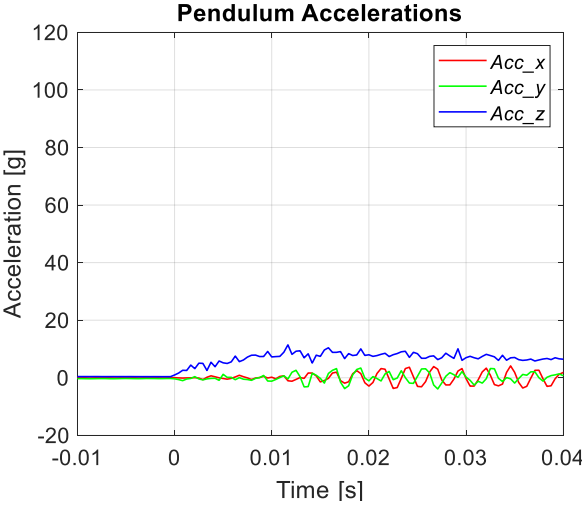

Fig. 30: Impact acceleration, boulder impact w/o face sheet (v=3m/s)

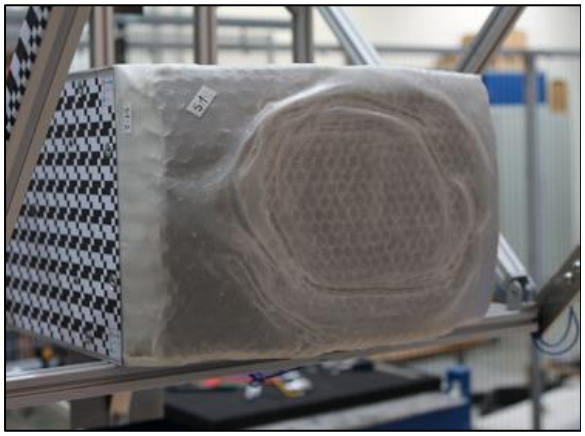

Fig. 31: Crash-pad with face sheet after impact with a hard flat surface (v=4m/s)

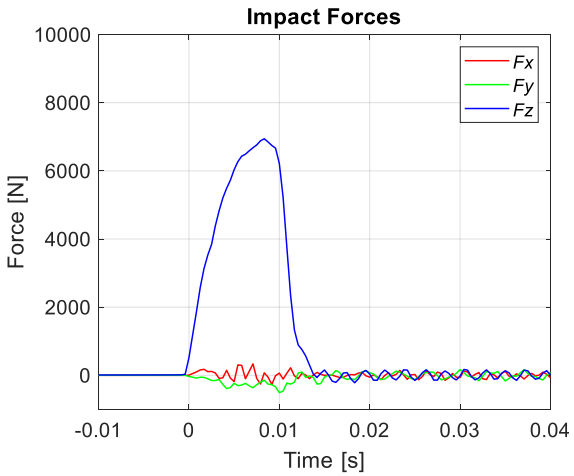

Fig. 32: Impact force, flat impact with face sheet (v=4m/s)

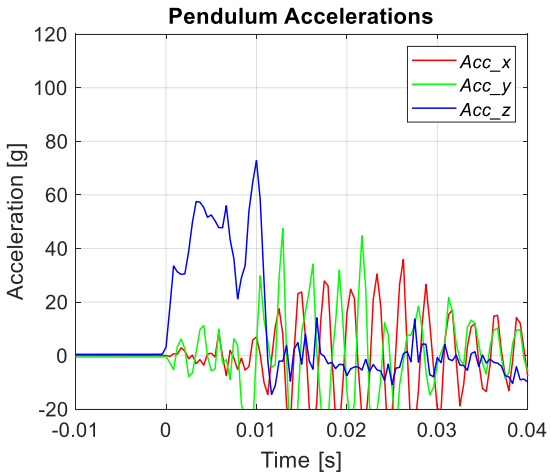

Fig. 33: Impact acceleration, flat impact with face sheet (v=4m/s)

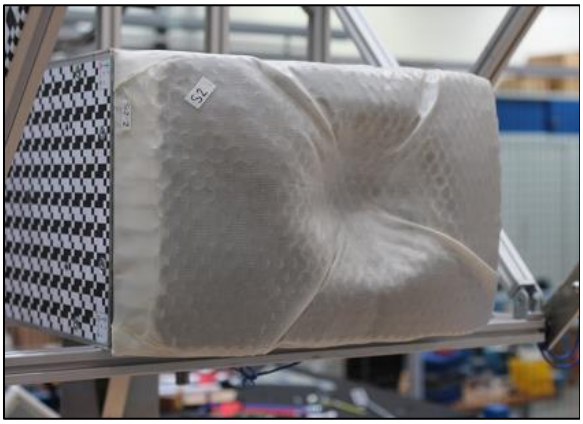

Fig. 34: Crash-pad with face sheet after impact with a hard obstacle/boulder (v=4m/s)

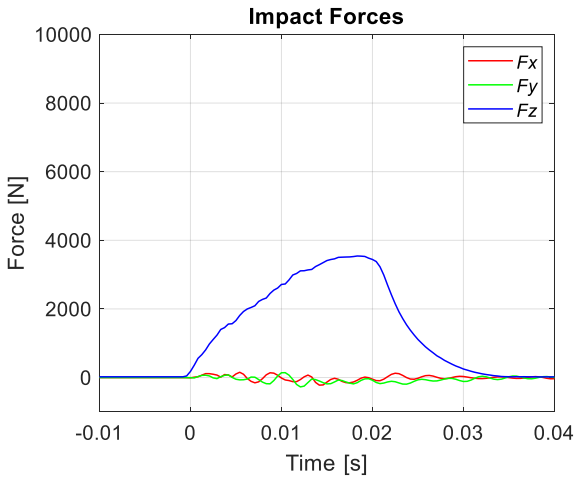

Fig. 35: Impact force, boulder impact with face sheet (v=4m/s)

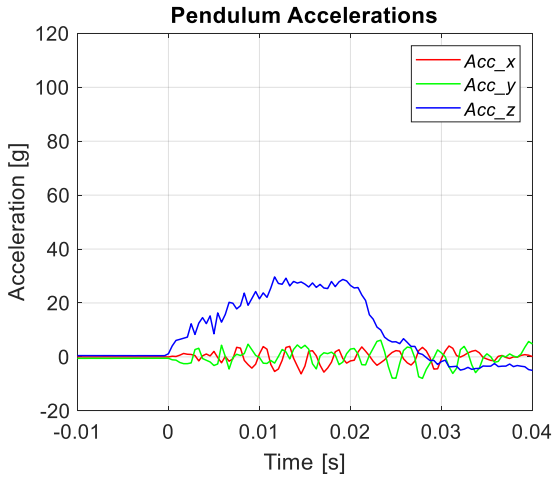

Fig. 36: Impact acceleration, boulder impact with face sheet (v=4m/s)

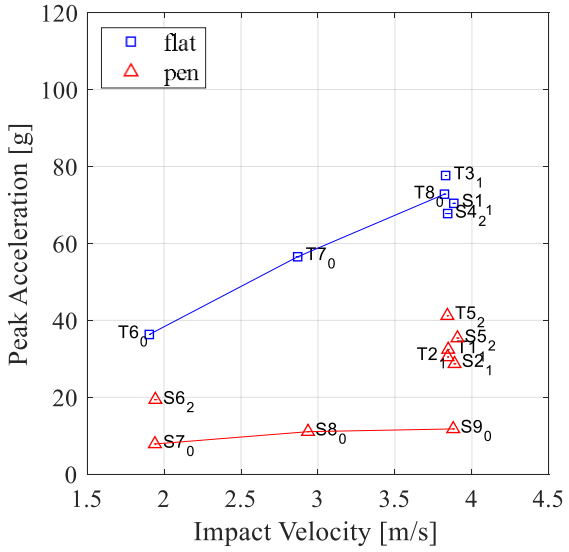

Fig. 37: Peak acceleration wrt impact velocity

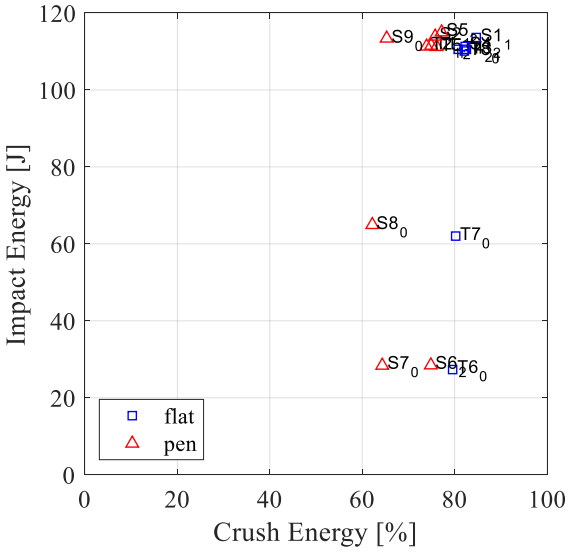

Fig. 40: Relation between impact energy and crush energy

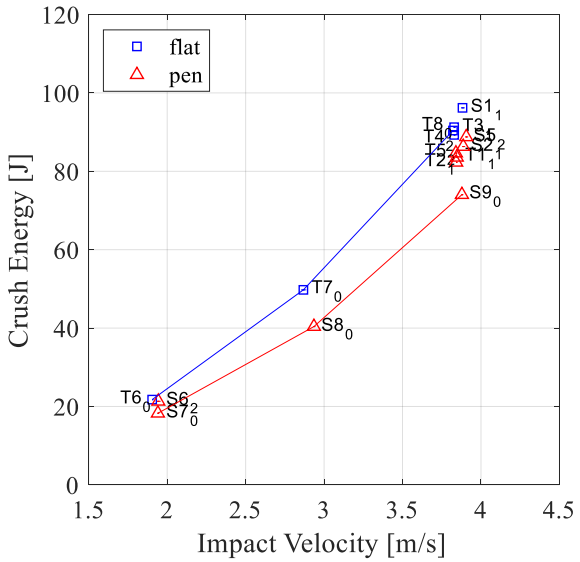

Fig. 38: Crush energy wrt impact velocity

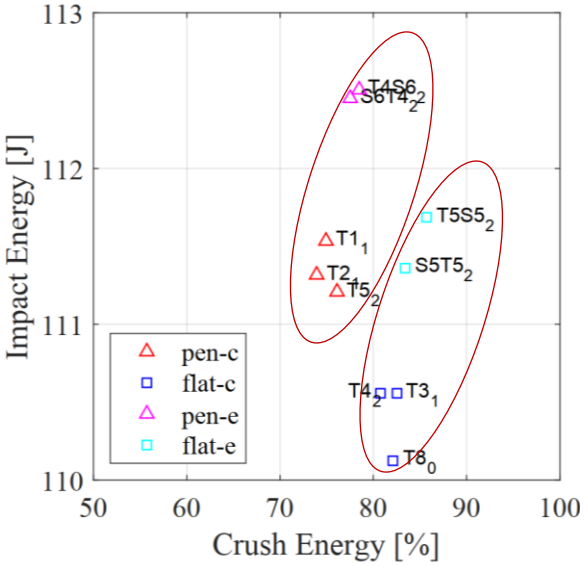

Fig. 41: Comparison of impact and crush energy for a central and edge impact

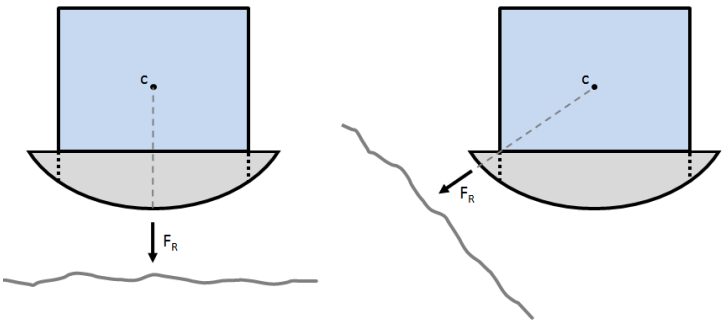

Fig. 39: Left: Worst case central impact. Right: Worst case edge contact

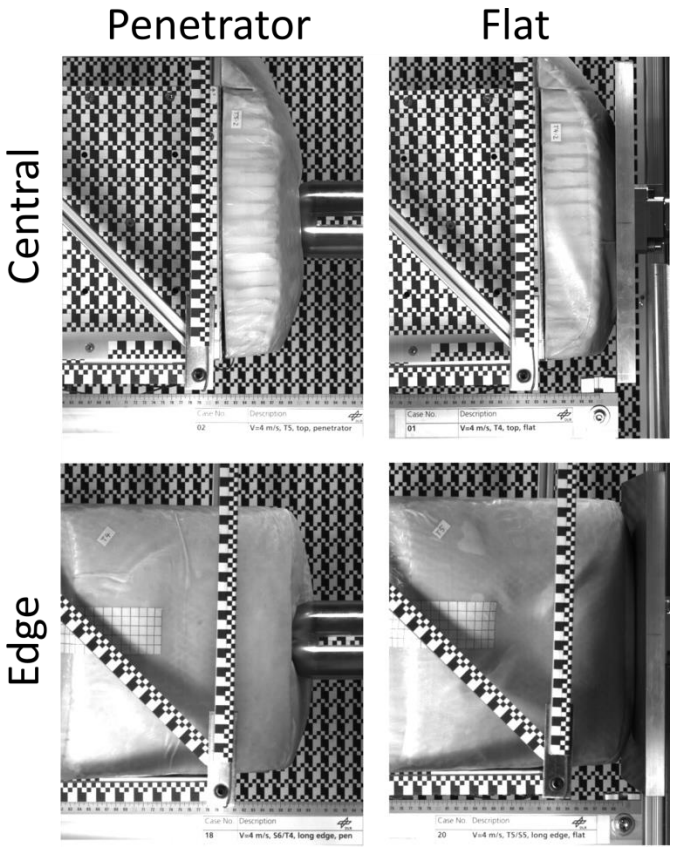

Fig. 42: Comparison of central and edge impact. Top-left: Penetrator central impact (v=4m/s); Top-right: Flat central impact (v=4m/s); Bottom-left: Penetrator edge impact (v=4m/s); Bottom-right: Flat edge impact (v=4m/s).

9. Landing Simulation

If however, the lander impacts a feature at its edge, but the velocity vector is not parallel with the line joining the contact point and center of mass, the shell may absorb little energy and the collision induces a significant uncontrolled rotation during the rebound. The lander then could impact a rock on an unprotected side at a speed larger 1 m/s which would be sufficient to cause at least some damage. To address this as well as other possible critical scenarios this section will outline the development of a multi-body landing simulator.

Finite element analysis provides a detailed insight into the shell deformation and the resulting load distribution complementary to the impact tests. On the other side, multibody dynamic simulation gives insight into the interplay between the three principle elements, which are the lander itself, its ejectable shell and the planetary surface as well as the contact forces and constraints between them. This type of analysis is used to set up a high-fidelity landing simulator using the multibody simulation tool SIMPACK [42]. To investigate the contact conditions between (i) the shell and the terrain and (ii) and potential collisions between the shell and the lander body a contact and collision detection law [43] as part of the multibody dynamics simulation is used. The parametrization of the simulation model considers mass and stiffness properties of MASCOT-1 and the shell as shown in the previous chapter. The planetary surface is modelled as a 10 m x 10 m zone with a grid resolution of 0.025 m in a face-vertex format. This generic, virtual terrain is covered with boulders to allow studies of the lander response to user defined, varying fractional area coverages. The terrain model represents boulder size frequency distributions (BSFD) of the form $\boldsymbol{N_c \propto D^{-p}}$, whereas $\boldsymbol{N_c}$ is the cumulative number of boulders, D their diameter and $\boldsymbol{p}$ = 2.5±0.5 the scale factor. This scale factor is remarkably constant for otherwise very different small bodies as shown in a meta study [44] collecting insitu observations on BSFD of previously visited bodies Eros, Itokawa and Phobos. A value of $\boldsymbol{p}$ = 2.5 has been used in this study as a proxy for a realistic scenario with regard to obstacle situation. The virtual terrain generation follows a procedure developed and reported by [45] to explicitly study landing risks for small body landers. The fractional boulder coverage $\boldsymbol{F = f(D_{min}, p)}$ is user defined for purpose of studying system responses to increasing blockiness. The size range of boulders is selected purposefully in the same order of magnitude of the shell lander as smaller obstacles become too small to fully penetrate the shell or larger obstacle become too large to be regarded as

a penetrator at all. The surface is considered as rigid, hence no energy absorption contribution by the soil is assumed. The planetary body is assumed to be Phobos, hence the gravity is set to $6 \cdot 10^{-3} m/s^2$.

The following event sequence (Fig. 43) illustrates an example simulation with an initial touchdown velocity of 2.5 m/s. The boulder coverage in this illustration is 30%. Touchdown occurs at Fig. 43, t = 0.0 s onto a couple of small boulders (close-up image, Fig. 44). The lander bounces off with a residual velocity of ~ 0.5 m/s and ~ 4% of its initial kinetic energy respectively. The angular momentum due to eccentric impact loads exceed the stabilizing momentum of the fly wheel by orders of magnitude hence after touchdown (Fig. 43, t = 2.0 s). It tumbles as it gained angular momentum which could not be counteracted by the stabilizing flywheel, whose purpose is on stabilization against small disturbances encountered between deployment from the orbiter until this initial touchdown. The spent shell is shed 5.6 s after impact (Fig. 43, t = 5.6 s). The firing of the hold down and release mechanism reliefs the preload and causes the shell being kicked out of its restraint position. Both the lander and the shell continue on their individual ballistic flight subsequently shown in Fig. 45. In this simulation example the shell makes a second surface contact after release and is deflected by the terrain towards the lander. This happens at ~114 s and several 10m off after the first impact.

This simulation example is selected to highlight two potential risks: (i) the risk of unwanted re-contact and collision of the lander with its shell, and (ii) the risk from multipoint contacts (simultaneous contacts at different points of the shell's surface) between the shell and the boulder-strewn terrain during initial touchdown. The latter one results from the shape design of the shell – refer back to Fig. 16– which allows reducing the acting mass effectively when being hit eccentric. In the presence of boulder multipoint contacts – as seen in this simulation example above – a free motion of the impacting lander might be blocked (but not necessarily).

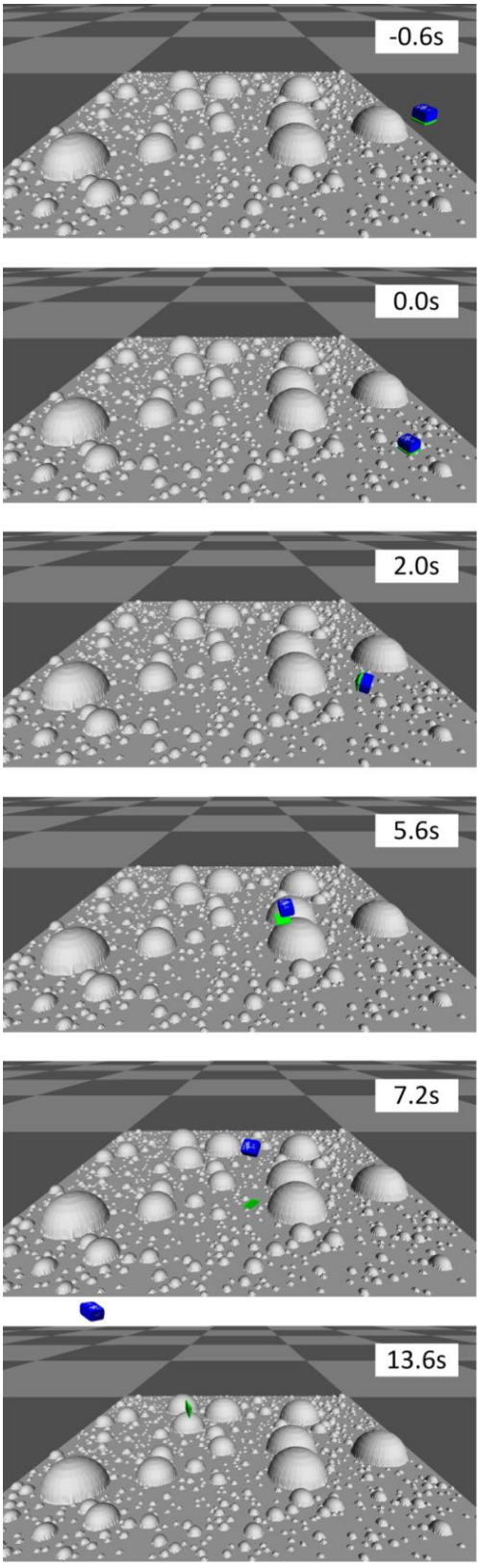

Fig. 43: Multibody simulation example (lander marked blue, shell in green), touchdown on terrain with 30% boulder coverage, main events: initial touchdown at t=0.0s, shell shedding at t=5.6s, shell rebound at t=7.2s

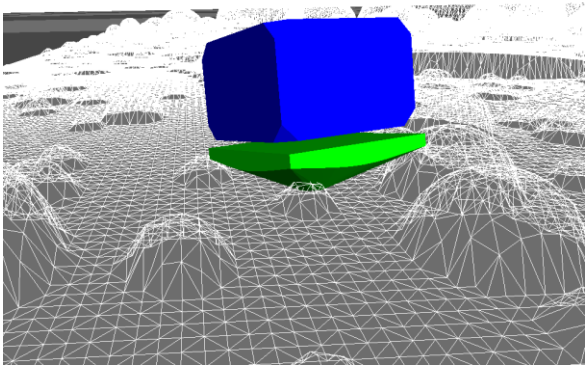

Fig. 44: Close-up of touchdown condition of the multibody simulation example. Both terrain surface and lander's shell contour are resolved in a face-vertex representation allowing evaluation of the contact conditions during the simulations run-time

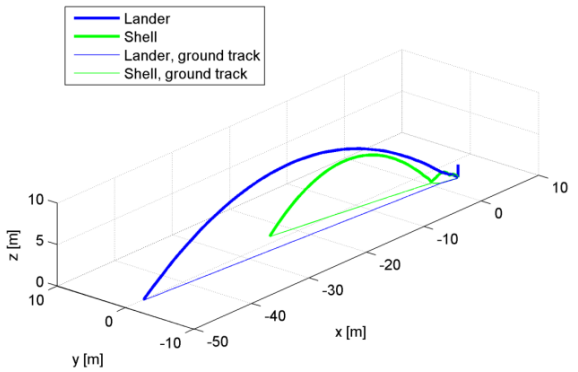

Fig. 45: Simulation example: lander and shell trajectories from initial touchdown until subsequent surface contacts

To assess the frequencies of occurrence of collisions between shell and lander and multipoint contacts the simulator has been used to run Monte-Carlo studies with each 800 simulated landings on terrains with boulder coverages of $\boldsymbol{F}$ = 10%, 30% and 50% respectively. Multipoint contacts have been observed in 18%, 34% and 42% of the cases. This result highlights a significant susceptibility to such events. The simulator is however not indicative to the actual vulnerability to these contact situations mandating further analysis for its mitigation and/or avoidance. The other potential harmful event of collisions between the lander and the spent shell has not been observed in any landing case and regardless of the boulder coverage.

In addition, Monte-Caro data sets have been evaluated with respect to the kinetic energy in translation/rotation mode at second impact. Fig. 46 shows the cumulative frequency of the total energy after impact. Data curves show results for different degrees of boulder coverages from 10% to 50%. Generally it can be said, that landings into lower degree of boulder coverage tend to result to lower residual energies. However, the increase from 30 to 50 is not as large as from 10 to 30. A closer look into the modes of residual energy is given in the smaller inlay at Fig. 46 which shows the share of total residual energy between translation and rotation. The share of rotational energy increases nearly linearly with large degree of bolder coverage but remains in a range between 1/5 and 1/3 of total.

The question what causes landings with relatively high residual kinetic energy or what makes energy absorption at first inherent is addressed by Fig. 47. In this figure the total kinetic energy is plotted over the number of contact points (see also explanation "multi-point contacts" above). This shows that with increasing number of simultaneous contact points the residual energy after such contact is generally lower. Higher levels of residual energy are seen when only a single contact occurs. Nevertheless, in this group the majority of landings stay within the low energy regime while the height of the column is determined by relatively few high energy landings.

A closer look into these individual landings reveals these cases are caused by "grazing shots" onto towering obstacles like cliffs or pronounced boulders as exemplarily shown in Fig. 48. These kinds of landings obviously poise a risk at the payload delivery as it decreases the absorption efficiency of the landing system. However, such "single point contacts" are mostly hits on unobstructed terrain. In addition, the mitigation of this risk is specific to the actual system and mission design and has two options:

i) Landing site selection, which avoids towering obstacles at large, or if not possible,

ii) Protect the payload entirely with the proposed shell concept such as depicted in Fig. 13

It shall be pointed out that the sole purpose of this simulation is to verify the functionality of the proposed lander concept between the initial and from shell performance most critical contact and subsequent shell separation. An accurate analysis of the dispersion pattern of the final rest positions would mandate a simulator upgrade to consider soil effects, slope and inclination factors of the terrain patches and gravity field disturbances.

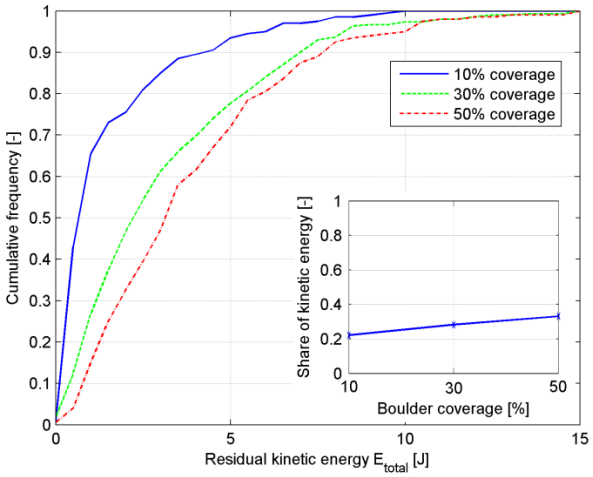

Fig. 46: Cumulative frequency of the total energy after impact. Initial kinetic energy is always 30.2 J. Inlay: share of total residual energy between translation and rotation.

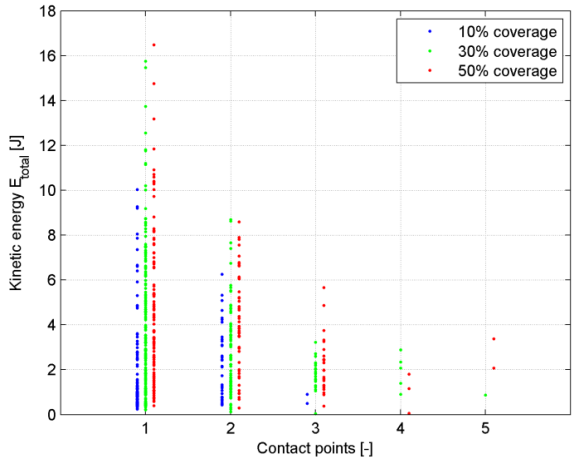

Fig. 47: Total kinetic energy plotted over number of contact points. Initial kinetic energy is always 30.2 J

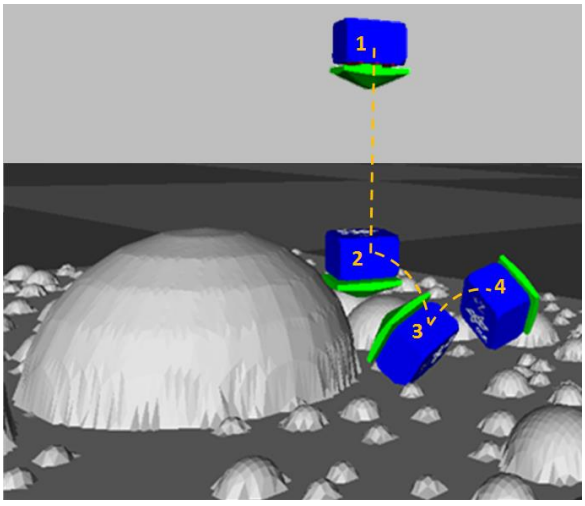

Fig. 48: Simulation example of a "grazing shot" onto towering obstacle: 1. initial inbound condition, 2. first contact with boulder, 3. second contact with surface, 4. outbound condition

10. Conclusions

Small carry-on landers have proven to be valuable assets by avoiding additional complexity of the main satellite and transferring the risk (and cost) of close surface maneuvers entirely or at least to some extend to an independent deployable system. In order to enable the exploration and landing on medium-size airless bodies between diameters of 10 - 50 km we presented in this paper the idea of advancing carry-on landers with a crushable-shell protection system to sustain higher landing velocities in the range of 1 - 5 *m/s*. For this, we first classified carry-on landers with respect to their touchdown and operational strategy to find similarities and identify key technologies. We evaluated the constraints of ballistic deployments for different target bodies as well as identified the niche for using simple honeycomb impact dampers compared to optional retro-propulsion systems. Further, we introduced the system design of an attitude-stabilized Shell Lander using a generic instrument carrier attached to a single ejectable crash-pad with stabilizing capability to protect the instrument carrier from structural damage, limit internal shock loads for sensitive payloads as well as reduce the amount of bounces on the surface. Design rules for material selection and shape optimization have been derived from analysis and experimental investigations. A mission architecture for a reference case to the Martian moon Phobos has been presented which provided a proof of concept based on laboratory impact tests. And finally, a landing simulator has been developed to numerically analyze the concept of operations from touchdown to terrain interaction, shell-shedding and landing. Monte-Carlo landing analysis shows that the shell can be safely separated and the likelihood of a harmful interference with lander is extremely low. Landing in rugged terrain inevitably causes multipoint contacts whose potential detrimental effect in conjunction with the optimized shell curvature yet needs to be investigated. Mitigation – if found necessary – would be specific to an actual mission design and could be either an engineering constraint on the landing site selection by implying a limit boulder coverage. Or it could mandate an increase in shell thickness to adapt to particular rough terrain.

References

[1] Biele, J., Ulamec, S., Maibaum, M., et al., *The landing(s) of Philae and inferences about comet surface mechanical properties*, Science 349(6247) aaa9816, 2015

[2] Grimm, C., Grundmann, J.-T., Hendrikgs, J., et al., *From idea to flight - A review of the Mobile Asteroid Surface Scout (MASCOT) development and a comparison to historical fast-paced space programs*, Progress in Aerospace Sciences, vol. 104, p. 20-39, 2019

[3] Grimm, C., Lange, C., Lange, M., et al., *The MASCOT Separation Mechanism – A reliable, low-mass deployment system for nano-spacecraft*, CEAS Space Journal, 2020

[4] Michel, P., Cheng, A., Küppers, M., et al, *Science case for the Asteroid Impact Mission (AIM): A component of the Asteroid Impact & Deflection Assessment (AIDA) mission*, Advances in Space Research 57(12) 2529-2547, 2016

[5] Michel, P., Cheng, A., Küppers, M., et al, *The HERA Mission: European Component of the Asteroid Impact and Deflection Assessment (AIDA) Mission to a Binary Asteroid*, 49th Lunar and Planetary Science Conference 2018 (LPI Contrib. No. 2083)

[6] NASA Space Science Data Coordinated Archive (NSSDCA), *NASA's Discovery Program*, https://nssdc.gsfc.nasa.gov/planetary/discovery.html, (accessed 16.05.2018).

[7] NASA Space Science Data Coordinated Archive (NSSDCA), NASA Science Missions, https://science.nasa.gov/missions-page?field_division_tid=81&field_phase_tid=All&=Apply, (accessed 15.09.2018).

[8] Beshore, E., Lauretta, D., Boynton, W., et al., *The OSIRIS-REx asteroid sample return mission*. In: 2015 IEEE Aerospace Conference pp. 1-14. IEEE.

[9] Kane, V., *Proposals to Explore the Solar System's Smallest Worlds*, 27 July 2015, http://www.planetary.org/blogs/guest-blogs/van-kane/20150727-proposals-to-explore-the-solar-systems-smallest-worlds.html, (accessed 09.2018).

[10] Staehle, R. L., Blaney, D., Hemmati, H., et al., *Interplanetary CubeSats: Opening the Solar System to a Broad Community at Lower Cost*, Journal of small satellites: research, technology, and systems, 2(1) 161-186, 2013

[11] Lange, C., Ho, T., Grimm, C., et al., *Nanoscale landers and instrument carriers: enhancing larger mission's science return by investing in low cost solutions: the MASCOT-1 to X and ROBEX examples*, In: 11th Low Cost Planetary Missions Conference, Berlin, Germany, 2015

[12] Adams, E., Hohlfeld, E., Hill, S., et al., *Asteroid in situ exploration using planetary object geophysical observer (POGO)*, In: 2016 IEEE Aerospace Conference, pp 1-10,

[13] Reid, R. G., Roveda, L., Nesnas, I. AD, et al., *Contact dynamics of internally-actuated platforms for the exploration of small solar system bodies*, In: Proceedings of i-SAIRAS, pp.1-9, Montreal, Canada, 2014

[14] Hockman, B. J., Frick, A., Reid, R. G. et al., *Design, Control, and Experimentation of Internally-Actuated Rovers for the Exploration of Low-gravity Planetary Bodies*, Journal of Field Robotics 34(1) 5-24, 2017

[15] Ho, T., Lange, C., Grimm, C., et al., *A Mobile Asteroid Surface Scout for the AIDA Mission*, In. EGU General Assembly, vol.18 p.16163, Vienna, Austria, 2016

[16] Ho, T., Biele, J., Lange, C., et al., *AIM MASCOT-2 Asteroid Lander Concept Design*, 20 February 2016, ESA General Studies Programme, https://gsp.esa.int/gsp-study-view/-/wcl/gaUaMHco1QJ9/10192/aim-mascot-2-asteroid-lander-concept-design, (accessed 15.09.2018).

[17] ESA, *Small Planetary Platforms (SPP) Executive Summary*, CDF Study Report, CDF-178(C), January 2018

[18] Ball, A., Garry, J., Lorenz, R., Kerzhanovich, V., *Planetary landers and entry probes*, Cambridge University Press, 2007

[19] Yano, H., Kubota, T., Miyamoto, H., et al., *Touchdown of the Hayabusa spacecraft at the Muses Sea on Itokawa*, Science 312(5778) 1350-1353, 2006

[20] Yoshimitsua, T., Kubota T., Nakatani I., et al., *Micro-hoppingrobot for asteroid exploration*, Acta Astronautica 52(2-6) 441-446, 2003

[21] NASA Space Science Data Coordinated Archive (NSSDCA), Phobos-Grunt, NSSDCA/ COSPAR ID: 2011-065A, https://nssdc.gsfc.nasa.gov/nmc/spacecraftDisplay.do?id=2011-065A, (accessed 07.05.2018).

[22] Watanabe, S., Tsuda, Y., Yoshikawa, M., et al., Hayabusa2 Mission Overview, Space Science Reviews 208(1) 3-16, 2017

[23] NASA Space Science Data Coordinated Archive (NSSDCA), OSIRIS-REx, NSSDCA/ COSPAR ID: 2016-055A, https://nssdc.gsfc.nasa.gov/nmc/spacecraftDisplay.do?id=2016-055A, (accessed 16.05.2018).

[24] JAXA, Martian Moons eXploration (MMX) Mission Overview, www.isas.jaxa.jp/en/topics/files/MMX170412_EN.pdf, (accessed 15.09.2018).

[25] Hockman, B. J, Pavone, M., *Stochastic Motion Planning for Hopping Rovers on Small Solar System Bodies*, In: Proceedings of ISRR, 2017.

[26] Hockman, B. J., Frick, A., Reid, R. G., et al., *Design, Control, and Experimentation of Internally-Actuated Rovers for the Exploration of Low-gravity Planetary Bodies*, Journal of Field Robotics, 34(1), 5-24, 2017

[27] Witte, L., *Touchdown Dynamics and the Probability of Terrain Related Failure of Planetary Landing Systems*, Universität Bremen, 2015

[28] Hexcel Corporation, *HexWeb CR III Product Data Sheet*, 2017 [www.hexcel.com, accessed 04.09.2018]

[29] Lemmer, K., *Propulsion for CubeSats*, Acta Astronautica 134, p. 231-243, 2017, doi:10.1016/j.actaastro.2017.01.048

[30] X. Yu and J. Zhou, *CubeSat: A candidate for the asteroid exploration in the future*, 2014 International Conference on Manipulation, Manufacturing and Measurement on the Nanoscale (3M-NANO), Taipei, 2014, pp. 261-265. doi: 10.1109/3M-NANO.2014.7057349

[31] Krasinsky, G. A., Pitjeva, E. V., Vasilyev, M. V., et al., *Hidden Mass in the Asteroid Belt*, Icarus 158(1) 98-105, 2002

[32] Weissman, P. R., Lowry, S. C., *Structure and density of cometary nuclei*, Meteoritics & Planetary Science 43(6) 1033-1047, 2008

[33] Lange, C., Ho, T. M., Grimm, C. D., et al. *Exploring Small Bodies: Nanolander and–spacecraft options derived from the Mobile Asteroid Surface Scout*. Advances in Space Research, 2017

[34] Bibring, J. P., Rosenbauer, H., Boehnhardt, H., et al., *The ROSETTA lander ("PHILAE") investigations.* Space science reviews, 128(1-4), 205-220, 2007

[35] Back to Mars: 1988, Soviet Robots in the Solar System, November 3, 2015, http://ourairports.biz/?p=2955, (accessed 15.09.2018).

[36] The Final Soviet Debacle, 05 September 2018 (last update), Bedford Astronomy Club, Global Surveyor, https://www.astronomyclub.xyz/global-surveyor/the-final-soviet-debacle.html, (accessed 15.09.2018).

[37] Hoggett, R., *1983-7 – PrOP-F Phobos Hopper*, 13 December 2012, http://cyberneticzoo.com/walking-machines/1983-7-prop-f-phobos-hopper-soviet/, (accessed 15.09.2018).

[38] Schröder, S., Grimm, C., Witte, L., *A Crushable Shell for Small Body Landers*, In: Proceedings of DLRK 2018

[39] Schröder, S., Reinhardt, B., Brauner, C., et al., *Development of a Marslander with crushable shock absorber by virtual and experimental testing*. Acta Astronautica, 134, 65-74. 2017

[40] Schröder, S., Witte, L., van Zoest, T. *Applications for a Gracity Compensation Test Facility for Planetary Surface Mobility*, In: Proceedings of DLRK 2011

[41] Schröder, S., Biele, J., Block, J., et al., Philae *Landing Test at the Landing and Mobility Test Facility (LAMA).* In: Proceedings of the 64th International Astronautical Congress, 2013

[42] SIMULIA, SIMPACK Multibody Simulation Software – Overview, www.simpack.com , [accessed 15.11.18]

[43] Gerhard Hippmann, An Algorithm for Compliant Contact Between Complexly Shaped Bodies, Multibody System Dynamics, Volume 12, Issue 4, pp 345–362, 2004, doi: 10.1007/s11044-004-2513-4

[44] Carolyn M. Ernst et.al, Evaluating Small Body Landing Hazards Due To Blocks, 46th Lunar and Planetary Science Conference, Abstract 2095, 2015

[45] Rodgers, D.J. et.al, Methodology for finding and evaluating safe landing sites on small bodies, Planetary and Space Science (2016), doi: 10.1016/j.pss.2016.10.010

[46] Biele, J., Grimm, C., Schroeder, .S, et al. „Experimental Determination of the Structural Coefficient of Restitution of a Bouncing Asteroid Lander", arXiv preprint arXiv:1705.00701. 2017.

[47] JAXA Hayabusa2 Project, "Asteroid explorer Hayabusa2 - Reporter briefing", September 24, 2019

[48] Yoshida, K. "Outline of the operation of MINERVA-II2 (Rover 2) deployment", September 24, 2019